# UNIVERSITY OF BUCHAREST

### MASTER THESIS

# Towards a real size Transition Radiation Detector prototype for the planned Compressed Baryonic Matter experiment

*Author:*
Dipl. Mădălina-Gabriela
Târzilă

*Supervisors:*
Prof. Dr. Mihai PETROVICI
Conf. Dr. Lucian ION

*This thesis fulfils the requirements for the degree of Master of Physics Faculty, Bucharest University*

*It was carried out in the "CBM Research and Development" group*

*of Hadron Physics Department*

*of the National Institute for Physics and Nuclear Engineering-Horia Hulubei, Bucharest, Romania*

June 27, 2013

# Declaration of Authorship

I, Mãdãlina-Gabriela TÂRZILÃ, declare that this thesis titled 'Towards a real size Transition Radiation Detector prototype for the planned Compressed Baryonic Matter experiment' and the work presented in it are the results of my own activity.

I confirm that:

- This work was done wholly or mainly while in candidature for a research degree at this University.

- Any part of this thesis has previously been submitted for a degree or any other qualication at this University or any other institution.

- Where I have quoted from the work of others, the source is always given.

- With the exception of such quotations, this thesis is entirely my own work.

- I have acknowledged all main sources of help.

- Where the thesis is based on work done by myself jointly with others, I have made clear exactly what was done by others and which was my personal contribution.

Signed:

_____

Date:

_____

UNIVERSITY OF BUCHAREST

Physics Faculty
Hadron Physics Department

Master of Physics Faculty

**Towards a real size Transition Radiation Detector prototype for the
planned Compressed Baryonic Matter experiment**

by Mãdãlina-Gabriela Târzilã

# *Abstract*

Three high granularity Transition Radiation Detector (TRD) prototypes for high counting rate environments, required by the CBM experiment at the future experimental facility FAIR, GSI-Darmstadt, were designed, built and tested. The present thesis is focused on the study of the electron-pion discrimination and position resolution capabilities of the these prototypes. Chapter 1 consists of an overview of the main theoretical arguments that motivate the construction of CBM Experiment and the experimental investigations which will be carried out using this experimental facility. Next chapter continues with a detailed description of the CBM experimental arrangement and of the current design of the CBM-TRD. The main physical phenomena underlying the detection and identification systems with a special focus on TRD are described in Chapter 3. In Chapter 4 construction details of the prototype architecture are presented for the small chambers as well as for the real size TRD. The prototypes were tested with an $^{55}$Fe radioactive source in the detector laboratory of the Hadron Physics Department of IFIN-HH and with a mixed beam of pions and electrons at CERN Proton Synchrotron. The experiments and the analysis methods which led to the obtained results concerning electron-pion discrimination and position resolution are presented in Chapter 5. The conclusions are summarized in Chapter 6.

# *Acknowledgements*

I would like to express my deepest appreciation to all those who have contributed to the successful completion of this thesis.

Foremost, I would like to express my sincere gratitude to my advisor Prof. Mihai Petrovici for the continuous support of my master study and research, for his patience, motivation, enthusiasm and immense knowledge. His guidance helped me in all the time of research and writing of this thesis.

Besides my advisor, I would like to thank Dr. Alexandru Bercuci for his help in the data analysis and a great deal of valuable advice. I'm also grateful to Dr. Mariana Petris for her advise and constructive comments on my analysis.

My sincere thanks also goes to all members of the "CBM Research and Development" group of Hadron Physics Department, my work would never be completed without their efforts at developing and constructing the TRD prototypes.

# Contents

# List of Figures

# List of Tables

# Chapter 1

# Theoretical overview

The idea that matter is made of some elementary constituents dates back to the 5th century B.C., when Democritus, a Greek philosopher, suggested that matter consists of unchangeable and indivisible entities, atoms (atomos (Greek) = indivisible) that constantly move around. According to him these atoms were made from the same type of material but had different shapes and sizes. However, it was not until the nineteenth century that this idea was picked up again.

In the early nineteenth century John Dalton used the idea of atoms to establish quantitative rules for chemical reactions. He proposed that all matter was composed of small indivisible particles termed atoms and suggested that atoms of a given element possess unique characteristics and weight. But even at that time, the atomic theory was not yet established and some still believed matter to be continuous without any substructure.

Only at the beginning of the twentieth century the atomic theory was firmly established by Einsteins paper on Brownian motion and soon thereafter Rutherford, Geiger and Marsden demonstrated by the scattering of $\alpha$-particles off gold foil that the atom contains a positively charged nucleus, where most of its mass is concentrated surrounded by negative charge electrons.

In 1932, the neutron was discovered and no doubt was left that the nucleus consists of neutrons and protons, the so-called nucleons. In addition to the electron, the proton, and the neutron, the neutrino was postulated in 1930 in order to reconcile the observations in $\beta$-decay with the conservation laws of energy, momentum, and angular momentum. Furthermore, in order to explain physical effects like nuclear decay and binding energy, new forces were postulated: the weak and strong interactions were introduced.

In accelerator experiments carried out during the 50s and 60s of the twentieth century, an abundance of strongly interacting particles and antiparticles, was discovered, the hadrons.

Hadrons are a large family of non-fundamental particles that can be subdivided into groups with similar properties. They were first only subdivided according to the particle weight into baryons (barys (Greek) = heavy) and mesons (mesos (Greek) = middle). The particles only interacting weakly or via the electromagnetic force were called leptons (leptos (Greek) = thin).

In 1964 Gell-Mann and Zweig introduced the idea that the hadrons with all their quantum numbers are built up from smaller entities, the quarks, with fractional charge and baryon number, which became the quark model. Using this model, all hadrons as well as their properties could be explained as combinations of two or three quarks.

## 1.1   Standard Model of Particle Physics

The Standard Model of particle physics is the theory of the elementary particles and three of the four known fundamental interactions between them. According to this model, the constituents of matter are six quarks and six leptons (see Table 1.1).

The three known fundamental forces described by the Standard Model are the weak nuclear force, the strong nuclear force and the electromagnetic force. The fourth one is gravitation and is not included in the Standard Model, however, for particle physics, when it comes to the small scale of particles, the effect of gravity is weak and thus can be neglected. It is postulated that gravitation is mediated by the exchange of a particle similar to the other three forces (see Table 1.2). These exchanged particles are called gauge bosons. Bosons are particles with integer spin and thus obey to Bose-Einstein statistics.

According to present knowledge quarks and leptons are considered elementary particles with spin 1/2, they obey Fermi-Dirac statistics, and are therefore called fermions. These fermions are considered as point-like particles and are grouped into three generations as shown in Table 1.1 adapted from Reference [1].

Each generation contains a charged lepton (the electron $e^-$, the muon $\mu$, and the tau $\tau$), the corresponding neutrino, which only interacts weakly, as well as two kinds of strongly interacting quarks. The associated antiparticles are identical in mass and spin but with opposite charge-like quantum numbers, such as charge, baryon or lepton number.

| Leptons | | | Quarks | | |
|---|---|---|---|---|---|
| **Symbol** | **Charge (e)** | **Mass** | **Symbol** | **Charge (e)** | **Mass** |
| $e^-$ | -1 | $0.511\text{MeV/c}^2$ | u | +2/3 | $(2.55)^{+0.75}_{-1.05}\text{MeV/c}^2)$ |
| $\nu_e$ | 0 | $<2\text{eV/c}^2$ | d | -1/3 | $(5.04)^{+0.96}_{1.54}\text{MeV/c}^2)$ |
| $\mu^-$ | -1 | $105.7\text{MeV/c}^2$ | c | +2/3 | $(1.27)^{+0.07}_{-0.9}\text{GeV/c}^2)$ |
| $\nu^\mu$ | 0 | $<190\text{eV/c}^2$ | s | -1/3 | $(101)^{+29}_{-21}\text{MeV/c}^2)$ |
| $\tau^-$ | -1 | $1.777\text{GeV/c}^2$ | t | +2/3 | $(172.0\pm2.2)\text{GeV/c}^2)$ |
| $\nu^\tau$ | 0 | $<182\text{eV/c}^2$ | b | -1/3 | $(4.19)^{+0.18}_{-0.06}\text{GeV/c}^2)$ |

TABLE 1.1: The Standard Model: the constituents of matter and their properties.

The quarks, classified into six different types or flavors called up (u), down (d), charm (c), strange (s), top (t), and bottom (b), and their anti-quarks allow the construction of most of the known hadrons, with a baryon containing a combination of three quarks ($qqq$) and a meson built up by a quark-anti-quark pair ($q\bar{q}$).

Quarks have a quantum number called color and come in three colors, which play the role of the charge for the strong interaction among quarks. The notion of this color charge was introduced to explain how quarks could coexist inside some hadrons in otherwise identical quantum states without violating the Pauli exclusion principle. This new quantum number is called color charge or color and each quark carries one of three colors: blue, red, or green.

| Force | Relative strength | Gauge bosons | Acts on |
|---|---|---|---|
| strong nuclear force | 1 | gluons | quarks |
| electromagnetic force | $\frac{1}{137}$ | photons | all charged particles |
| weak nuclear force | $\sim10^{-7}$ | $W^\pm$, $Z^0$ | quarks and leptons |
| gravitation | $\sim10^{-39}$ | gravitons | all massive particles |

TABLE 1.2: The Standard Model: fundamental forces. The strong nuclear force acts on the colour charge of the quarks like the electromagnetic force acts on charge. The gravitation is the only fundamental force that is not described by the Standard Model.

The quarks combine in such a fashion to make all baryons and mesons color neutral objects. In the highest energy scattering events quarks were never observed to exist outside of their parent hadrons. This indicated that the force between two quarks must increase as the distance between them increases. The presence of a massless particle to mediate the force between two quarks was introduced. This particle was referred to as a gluon. The gluon is the analogue to the photon, a massless boson that mediates the electromagnetic force between charged objects in Quantum Electrodynamics (QED). Unlike the photon, which carries no electric charge, the gluon cannot be neutral with respect to the color charge. Since they are coloured, gluons do not interact only with quarks, but also among themselves. Their coloured nature leads to gluon self-interaction.

Since color charge is a conserved quantity, and the emission or absorption of a gluon leads to a color change, gluons can be considered as a combination of color and anticolor. There are nine possible combinations of color-anticolor, which leads to the prediction that there should exist nine gluons. However, the ninth combination is actually a linear combination of all color-anticolor, and therefore colorless.

### 1.1.1 Quantum Chromodynamics

Quantum Chromodynamics (QCD) is the theory within the Standard Model that describes the strong interactions between quarks and gluons. QCD was developed as an extension of Quantum Electrodynamics (QED) via the imposition of a local SU(3) symmetry in 'color' space.

The most important difference between QCD and QED is that QCD is the non-abelian gauge theory and as a consequence has gluon self-interaction.

A feature of QCD is the momentum transfer $(Q)$ dependence of the strong coupling constant $\alpha_s(Q)$ which is expressed as:

$$\alpha_s(Q) \approx \frac{12\pi}{(33 - 2n_f) \cdot ln\left(\frac{Q^2}{\Lambda_{QCD}^2}\right)} \qquad (1.1)$$

Here, $n_f$ is the number of active quark flavours with quark mass less than $Q$ and $\Lambda_{QCD}$ is the scale parameter of the strong interaction ($\Lambda_{QCD} \approx 200 MeV$).

At a large momentum transfer $(Q > \Lambda_{QCD})$ and equivalently at a short distance, $\alpha_s(Q)$ decreases logarithmically, and quarks and gluons behave almost freely. This is called 'asymptotic freedom'. The feature of asymptotic freedom allows us to describe the strong interaction at large $Q^2$ in term of perturbation theory.

In contrast, $\alpha_s(Q)$ becomes large at small momentum transfer $(Q \approx \Lambda_{QDC})$, at long distance. Thus, the perturbative approach is not applicable. In this region, quarks strongly attract each other and form color neutral state such as mesons and baryons. This phenomenon is called as "color confinement". Because of this "confinement" feature of QCD, a single colored-quark has never been observed.

The effect of confinement can also be illustrated with the phenomenological potential for the strong interaction:

$$V_s = -\frac{4}{3}\frac{\alpha_s}{r} + kr \qquad (1.2)$$

where the first term dominates at small distances $r$ and is similar to the Coulomb potential. The second term is dominant at large distances and is associated with the confinement: the color field between a pair is restricted to a small tube or string because of the gluon-gluon interaction. When trying to separate two quarks the stored energy $kr$ increases and it is energetically more favourable to form a new pair. The result is that there are two shorter strings. Thus separating two quarks is not possible, only new, color-neutral particles are produced.

### 1.1.2 Quark-Gluon Plasma

The environment of extremely high temperature and/or density can also reduce $\alpha_s$. The color confinement may be broken with increase of the temperature and/or density of a many body system consisted of hadrons. This results in a phase transition from the confined nuclear matter (hadronic ordered phase) to the deconfined state where the hadrons start to lose their identity and a phase of weekly interacting quarks and gluons can be reached. Such a deconfined state was called Quark-Gluon Plasma (QGP) [2].

The deconfined phase can occur at high temperatures like those in the relativistic collision of two heavy nuclei or at high baryon densities like those that might be found at the center of neutron stars.

The MIT bag model gives a phenomenological description of quarks in hadrons: quarks are treated as massless inside a bag of finite temperature and as infinitely massive outside the bag [3]. In this model confinement results from the balance between the bag pressure, directed inward, and the stress arising from the kinetic energy of the quarks. If this balance is distorted and the pressure of the quarks is larger than the bag pressure, a new phase of matter containing deconfined quarks and gluons is formed.

To reach this new phase, two extreme scenarios can be considered:

1. a quark-gluon system in thermal equilibrium with a large temperature $T > T_c$, where the kinetic energy of the quarks and the gluons with corresponding pressure $P$ exceeds the bag pressure;

2. a system at $T = 0$ with high baryon density $n_B$ or baryo-chemical potential $\mu_B$, where the Pauli principle forces the quarks into states with increasing momentum as they get closer, leading to a degenerative pressure that may exceed the bag pressure.

In other words, the two states of matter can be separated by the critical temperature, $T_c$ which is predicted by many simple models (e.g. the bag model) and also by lattice QCD calculations.
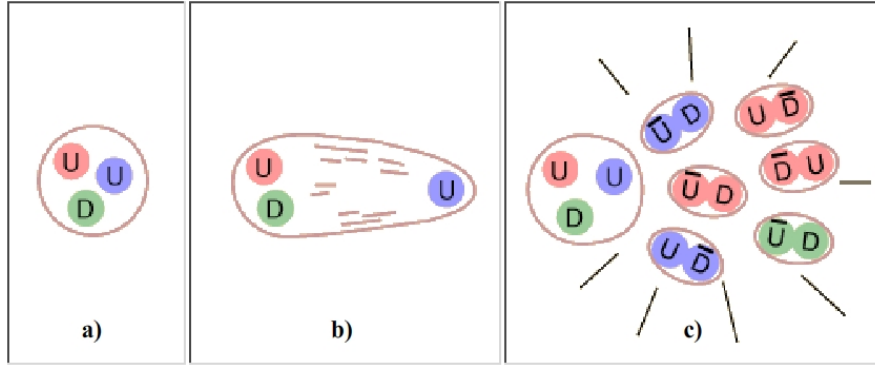
FIGURE 1.1: Model for quark confinement in a proton: a)The quarks of a proton are free to move within the proton volume; b)If you try to pull one of the quarks out, the energy required is on the order of 1 GeV per fermi, like stretching an elastic bag; c)The energy required to produce a separation far exceeds the pair production energy of a quark-antiquark pair, so instead of pulling out an isolated quark, you produce mesons as the produced quark-antiquark pairs combine [3].

Fig.1.2, from reference [4], shows a conceptual drawing of the two states of the matter consisting of quarks and gluons at higher temperature and confined hadronic matter at lower temperature relative to the $T_c$.
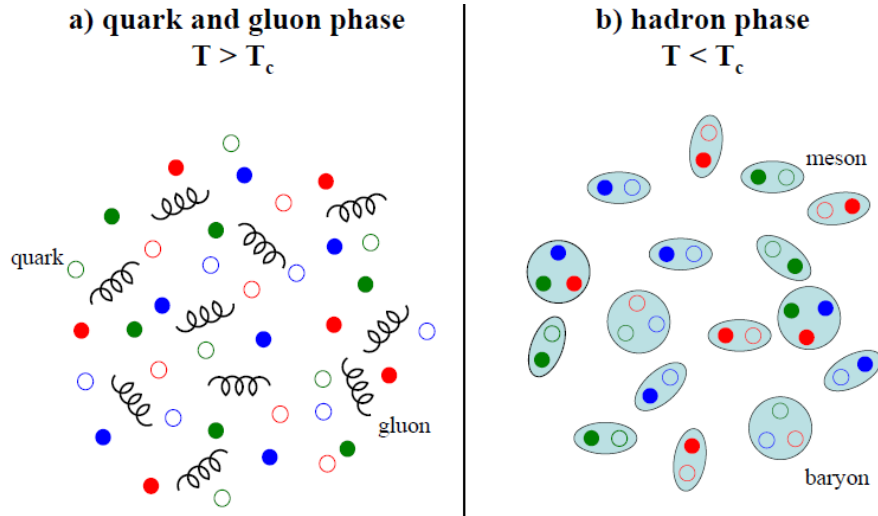


FIGURE 1.2: Conceptual drawing of matter that consist of quarks and gluons. a) Matter is in $T > T_c$. b) Matter is in $T < T_c$, quarks are confined in hadrons [4].

The different phases of QCD are illustrated in the phase diagram of strongly interacting matter. The schematic phase diagram of QCD matter is shown in Fig.1.3 in the plane of temperature $T$ and baryo-chemical potential $\mu_B$.

Lattice QCD calculations at vanishing baryo-chemical potential and finite temperature predict confinement above energy densities of about 1 GeV/fm$^3$ [5]. Such conditions may be created in central collisions between heavy nuclei already at bombarding energies of about 10 AGeV [6, 7]. Recent lattice QCD calculations at finite baryon chemical

potential predict a critical endpoint of deconfinement phase transition at $\mu_B \approx 400 MeV$ and $T \approx 160 MeV$ [8, 9].
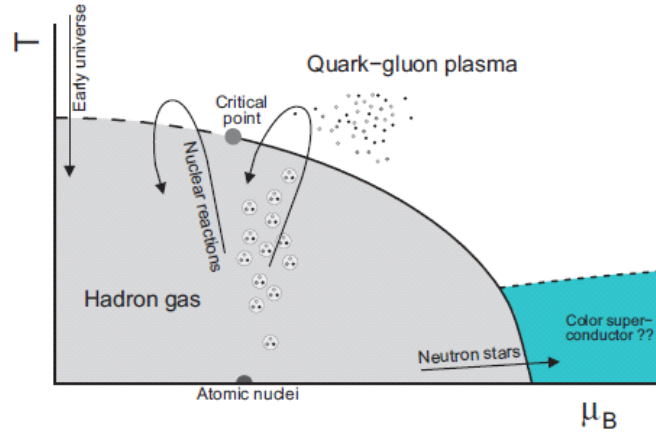


FIGURE 1.3: Schematic phase diagram of QCD [10]. The solid line indicates the first order phase transition from hadronic matter to the quark-gluon plasma. The dashed line at small baryon density represents a crossover transition.

Based on the fundamental property of asymptotic freedom, one expects at least three different regions:

- the hadronic phase at low $\mu_B$ and low $T$ ;

- the deconfined matter at high $T$ or moderate T and large baryonic chemical potential (baryon density);

- the color-superconducting region at high $\mu_B$, low $T$.

The current knowledge on the QCD phase diagram is illustrated in Fig.1.4. The data points correspond to chemical freeze-out and result from a statistical analysis of particle ratios measured in Pb+Pb and Au+Au collisions at SIS, AGS, SPS and RHIC [11].

The solid curve along the freeze-out points represents a calculation with a constant baryon density (baryons + antibaryons) of about $\rho_B = 0.75\rho_0$ [12]. The phase boundary between quark-gluon matter and hadronic matter together with the location of the critical endpoint as shown in Fig.1.4 is predicted by lattice QCD calculations [8, 9]. These calculations indicate that for values of $\mu_B$ larger than about 400 MeV the phase transition is first order, whereas for $\mu_B$ smaller than 400 MeV there is a smooth cross over from the hadronic to the partonic phase (dotted line). The confirmation of the critical endpoint is a real challenge of high-energy nucleus-nucleus collision experiments.

According to the calculations a beam energy of 10 AGeV is sufficient to cross the phase boundary. For a beam energy of about 30 AGeV the trajectory is predicted to pass the region of the critical endpoint of the deconfinement phase transition [13].
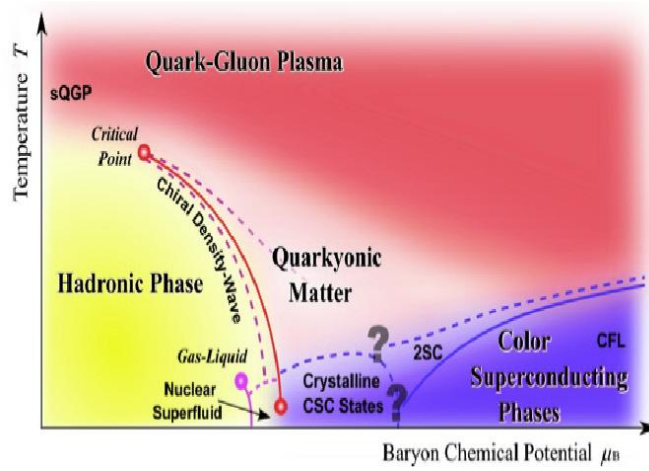
FIGURE 1.4: The phase diagram of strongly interacting matter plotted as a function of temperature and baryon chemical potential. The critical endpoint at $\mu_B \approx 400 MeV$ is predicted by lattice QCD calculations [12].

Enormous experimental and theoretical efforts have been and are still devoted to the search for the deconfined phase of strongly interacting matter, the quark-gluon-plasma (QGP). Experimental findings at SPS energies at CERN, like enhanced production of strangeness, anomalous suppression of charmonium, enhanced production of low-mass dilepton pairs, and the fact that an analysis of particle multiplicities yields a chemical freeze-out temperature of about 170 MeV which is very close to the critical temperature are very much in agreement with the expectations based on theoretical models inspired scenarios presented above. In which extend they are directly related to deconfined quark-gluon matter produced at these energies will be confirmed by the new generation of experiments at much higher energies going on at RHIC-Brookhaven and LHC-CERN.

The discovery of the critical endpoint of the deconfinement phase transition is the main research goal of the low energy scan program at RHIC and the next generation experiment CBM at FAIR and will be a direct indication for the existence of a new phase. Theoretical investigations suggest that particle density fluctuations occur in the vicinity of the critical endpoint, which might be observed experimentally as nonstatistical event-by-event fluctuations of observables. This phenomenon was also seen in lattice QCD calculations. The fluctuation signal should show up around a certain beam energy.

# Chapter 2

# The Compressed Baryonic Matter Experiment

## 2.1 Experiment overview

The Compressed Baryonic Matter (CBM) experiment at FAIR (Facility for Antiprotons and Ion Research), GSI [14], will investigate nucleus-nucleus collisions from 2 to 35 AGeV and explore the Quantum Chromo-Dynamics (QCD) phase diagram, shown in Fig.1.4, in the region of highest baryonic densities where the phase transition is expected to be, according to the Lattice QCD (LQCD) calculations, of first order. Moreover, the discovery of the critical endpoint-like region would be a breakthrough in high-energy heavy-ion research since this observation would confirm the phase-transition line.

The goal of the CBM experiment is to look in particular for rare probes by taking advantage of high intensity heavy-ion beams delivered by FAIR. CBM will be a multi-purpose experiment with the ability to measure leptons, hadrons, and photons. The CBM research area is complementary to the heavy-ion research program at RHIC and LHC.

The nucleus-nucleus collisions research program of CBM will focus on the search for [14]:

- in-medium modifications of hadrons in super-dense matter as signal for the onset of chiral symmetry restoration;

- a deconfined phase at high baryon densities;

- the critical endpoint of the deconfinement phase transition.

The program aims at a comprehensive study of relevant observables by systematically scanning experimental parameters like beam energy, system size and collision centrality.

The observables include:

- *open and hidden charm*: charm quarks are produced in the early phase of the collision and hence probe high-density baryonic or partonic matter. The sensitivity of charm production to medium effects is enhanced due to the fact that the beam energy is close to the threshold. Charmonium ($J/\psi$ mesons) will be measured via its decay into electron-positron (and muon) pairs, whereas $D$-mesons will be identified by the invariant mass of their hadronic decay products.

- *short-lived vector mesons decaying into electron-positron pairs*: The ultimate goal is the measurement of the in-medium spectral function of $\rho$(or $\omega$ and $\phi$) mesons in order to study effects of chiral symmetry restoration.

- *strange and multi-strange particles*: strangeness production plays an important role as a possible signature for a deconfined phase of strongly interacting matter produced in nucleus-nucleus collisions.

- event-by-event fluctuations of observables like particle ratios, charge ratios, mean transverse momentum, etc.: the search for the critical endpoint of the deconfinement phase transition requires large acceptance and good particle identification capability over a wide range of momenta and polar angles with close to uniform azimuthal coverage.

- photons: they offer the possibility to detect $\pi^0$ and $\eta$ mesons, and direct photons emitted in the early and dense phase of the collisions.

The experimental task is to identify both hadrons and leptons and to detect rare probes in a heavy ion environment. The apparatus has to measure yields and phase-space distributions of hyperons, light vector mesons, charmonium and open charm (including the identification of protons, pions and kaons) with a large acceptance. The challenge is to select very rare probes in Au+Au (or U+U) collisions at reaction rates of up to $10^7$ events per second. The charged particle multiplicity is about 1000 per central Au+Au event at 25 A·GeV. Such measurements require fast and radiation hard detectors, large acceptance and large granularity, electron and hadron identification ,fast and self-triggered read-out electronics, a high-speed data acquisition system, and online event selection based on full track reconstruction.

### 2.1.1 Detector layout

Two configurations of the CBM detector are envisaged: one is dedicated to the identification of electrons, while the other one is specialized in detecting muons. The current set-up for the two configurations is sketched in Fig.2.1.

Both designs have in common a low-mass silicon tracking system (STS), the core of the CBM experiment, used for charged-particle tracking, high resolution main and secondary vertex reconstruction and high-resolution momentum measurement with radiation tolerant silicon microstrip and pixel detectors. Combined with an ultra-thin micro-vertex detector (MVD) based on monolithic active pixel sensors, it will be installed in the gap of a dipole magnet in short distance downstream of the target, in general a Au foil of 250 $\mu$m thickness corresponding to 1% nuclear interaction length.
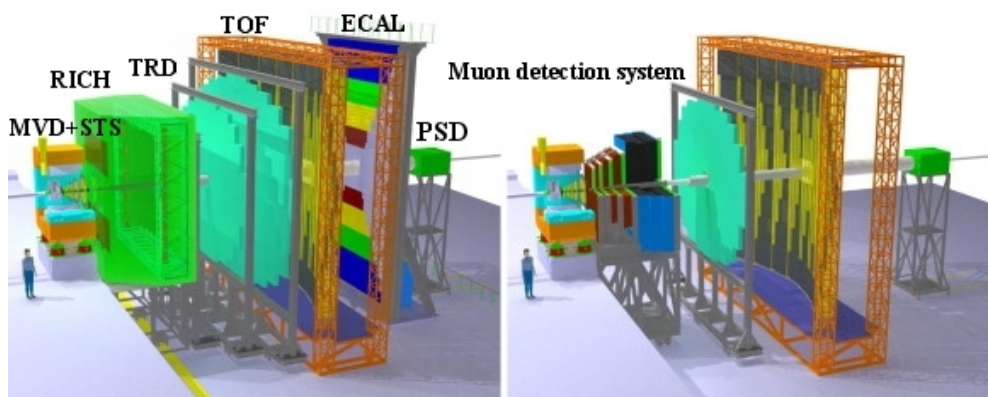


FIGURE 2.1: Schematic view of the CBM experiment: electron configuration (left side) and muon configuration (right side) [14].

In the electron configuration, the CBM experiment comprises a ring imaging Cherenkov (RICH) detector downstream of the magnet to identify electron-positron pairs from vector mesons decays. Three stations of transition radiation detectors (TRDs) provide charged particle tracking and identification of high energy electrons allowing to match tracks reconstructed in the STS to the TOF measurement. Hadron identification will be realized with a large-area time-of-flight detector (TOF) consisting of multi-gap resistive plate chambers (RPC). An electromagnetic calorimeter (ECAL) will be used to detect photons. The projectile spectator detector (PSD) is a calorimeter that determines the centrality and the reaction plane of the collisions measuring essentially the products emitted by the spectators.

In the muon configuration of the experiment, the RICH detector system will be replaced by a compact active absorber system (MUCH) for the measurement of charmonium via its decay into muon pairs. Both the MUCH and the RICH detectors will be

movable in order to be used alternatively for muon or electron measurements, respectively.

A particular feature of the experiment is its data acquisition and trigger concept, imposed by the physics programme with rare probes, e.g. charm production near threshold, and the necessity for interaction rates between 0.1 and 10 MHz. It is based exclusively on self-triggering front-end electronics that time-stamps the detector signals and ships them to a fast computing farm for event building and high-level trigger generation.

## 2.2 Transition Radiation Subsystem

The Transition Radiation Subsystem will provide electron identification and tracking of all charged particles. It has to provide, in conjunction with the RICH detector and the ECAL, sufficient electron identification capability for the measurements of charmonium and of low-mass vector mesons. The required pion suppression is a factor of about 100 and the position resolution has to be of the order of 200-300 $\mu$m.

In order to fulfil these requirements, in the context of the high rates and high particle multiplicities, a careful optimization of the sub-detectors geometry is required. The current design is shown in Fig.2.2: the detector is divided in three stations (summing up to a number of ten detector layers) positioned at distances of 4.5, 7.45 and 9 m from the fixed target. The whole detector can be assembled using two different modules: the inner region (polar angles between 50 and 200 mrad) of the eight first layers can be made of 60 x 60 cm$^2$ sized modules, the outer part of the layers can be build by modules of 100 x 100 cm$^2$ size (Fig.2.3), adding to 708 detector modules covering an area of 585 m$^2$, about 737.408 read-out channels.

The total thickness of the detector in terms of radiation length has to be kept as low as possible to minimize multiple scattering and conversions. To ensure the speed and also to minimize possible space charge effects expected at high rates, the active volume of each module has to have a thickness of about 1 cm.

Because of the high rate environment expected in the CBM experiment (interaction rates up to 10 MHz), an architecture specific for a fast readout detector has to be used. On the other hand, CBM being a fixed target experiment, the track density at low polar angles is quite high, therefore the size of the pads is chosen in a way that the expected hit rate per channel does not exceed 10 $^5$ Hz per channel. In the current geometry the pad size increases in radial direction from module to module from 1 cm$^2$ to 12 cm$^2$ (see Fig.2.3).
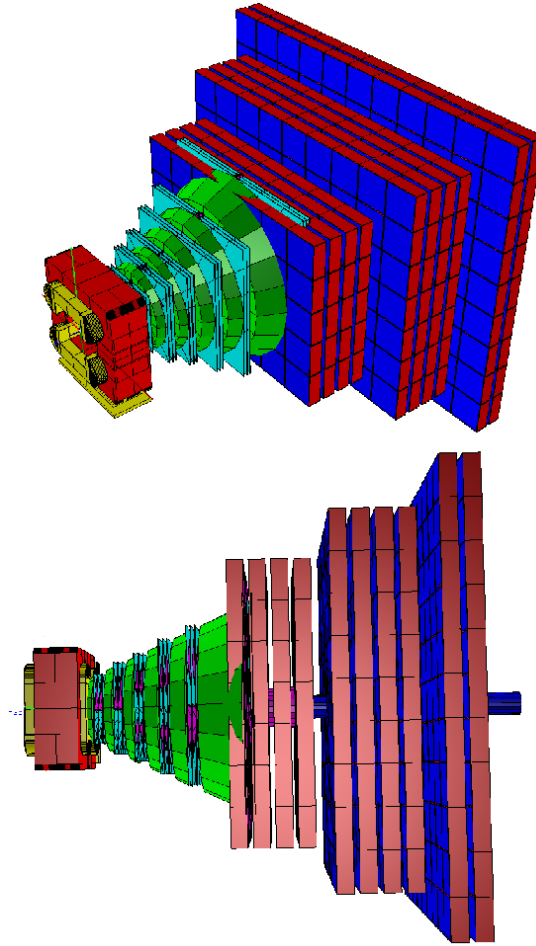
FIGURE 2.2: The geometry of the TRD subsystem consisting of 10 layers divided in 3 stations, developed in CbmRoot (CBM Simulation and Analysis Framework) [15].

For the radiator there are two possibilities: regular and irregular radiator (more details are presented in Chap.3.3.1). The regular radiator, composed of foils and gaps of equal size, would be the best choice as far as it provides the highest transition radiation yield, however, due to a complicated construction procedure the costs are rather high. The irregular radiator, composed of fibers, not stretched foils and/or foams has a reduced transition radiation yield compared to a regular radiator of the same material budget, but has the advantage to be easier manufactured and therefore much lower cost. The final choice of the radiator type will be established after the completion of prototypes tests using all type of radiators.

The gas mixture of the readout detectors will to be based on Xe, to maximize the absorption of transition radiation produced by the radiator.

To optimize the whole desing of the TRD subdetector, a detailed study of the tracking performance in combination with all the CBM subdetectors was started and is still ongoing.

FIGURE 2.3: Distribution of hit rate per pad for the first layer of each detector station [16].

# Chapter 3

# Detector Principle

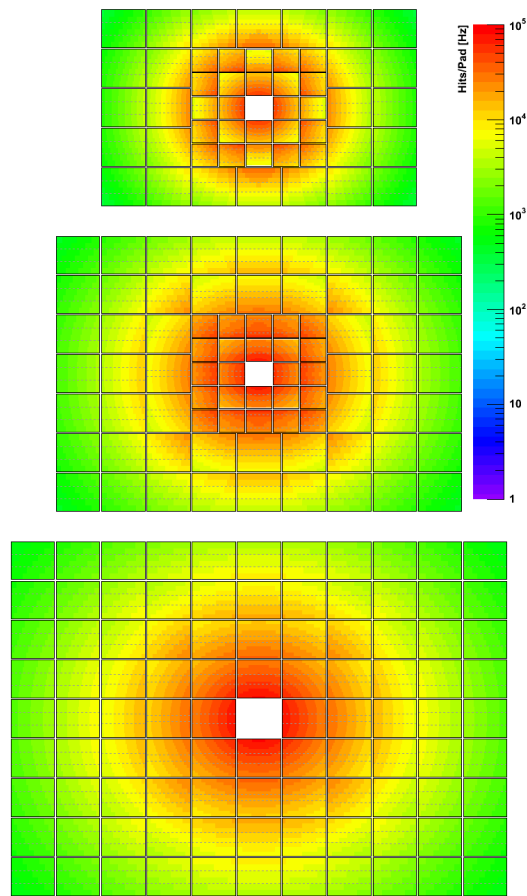Most particle detectors are based on the processes produced by particles and electromagnetic radiation in the matter they traverse. In the transition radiation detector two processes contribute to the signal that is used for particle identification:

1. charged particles deposit energy in the gaseous volume of the transition radiation detector - process described by the Bethe-Bloch formula;

2. charged particles produce, under certain conditions, transition radiation in the radiator material, the generated photons are absorbed in the detector gas, contributing to the signal.

When travelling through detector material, charged particles lose energy mainly by colliding with atomic electrons of the material (excitation and ionization) and by the emission of bremsstrahlung, i.e. "braking radiation" or "deceleration radiation", when they scatter atomic nuclei. In addition, hadrons can lose energy through hadronic interactions like inelastic nuclear collisions, or nuclear excitations.

Depending on their energy, photons can interact with atomic electrons of the detector material (Compton scattering or the photoelectric effect), or, if a minimum energy ($\geq$1.022 MeV) is reached, they convert into $e^+e^-$ (pairproduction).

## 3.1   Interaction of charged particles with matter

### 3.1.1   Energy loss of charged particles. The Bethe-Bloch formula

Charged particles deposit energy in a material caused by collisions with the atoms in the traversed material. This energy loss per unit of path length is described by the

Bethe-Bloch formula and is measured in keV/$\mu$m [17]:

$$-\frac{dE}{dx} = \frac{4\pi N e^4 z^2}{m_e c^2 \beta^2} \left( ln\frac{2 m_e c^2 \beta^2 \gamma^2}{I} - \beta^2 - \frac{\delta(\beta)}{2} \right) \tag{3.1}$$

where $N$ is the number density of electrons in the matter, $e$ is the elementary charge, $m_e$ represents the rest mass of the electron, and $c$ is the speed of light in the vacuum. The velocity of the traversing particle is given by $\beta = \frac{v}{c}$, and $\gamma = \frac{1}{\sqrt{1-\beta^2}}$ is the Lorentz factor, $z$ represents the electric charge of the particle, the mean excitation energy of the atoms of the traversed matter is described by $I$ (i.e. the energy required to ionize the atom), and $\delta$ is a correction factor for density effects.

The logarithmic term in the Bethe-Bloch equation varies slowly with velocity (and therefore with energy), so it is approximately correct, for very thin layers to write:

$$\Delta E = \left( -\frac{dE}{dx} \right) \Delta x \tag{3.2}$$

where $\Delta E$ is the average energy loss due to ionization and excitation in a layer of the medium with thickness $\Delta x$. The exact energy loss fluctuates around this average value. The energy fluctuations follow a Landau distribution for medium $x$ values. The distribution is roughly, but never perfect, Gaussian for a very thick medium, where the energy loss exceeds half of the original particle energy.

The above Bethe-Bloch formula describes correctly only the energy loss by ionization for muons and heavier particles. Since the mass of electrons and positrons is the same as the mass of the collision partner a correction has to be implemented. It can be shown that with this correction the mean of the deposited energy for electrons and heavier particles is the same for large values of $\gamma$ [17].

Relativistic particles lose energy not only due to ionization but also through the emission of bremsstrahlung, an electromagnetic radiation produced by the deceleration of charged particles (especially electrons) passing through matter in the vicinity of the strong electric fields of atomic nuclei. The energy loss results in the emission of photons.

Fig.3.1 describes the production of bremsstrahlung and of characteristic X-rays: events 1, 2, and 3 depict incident electrons interacting in the vicinity of the target nucleus, resulting in bremsstrahlung production caused by the deceleration and change of momentum, with the emission of a continuous energy spectrum of photons while event 4 demonstrates characteristic radiation emission, where an incident electron with energy greater than the K-shell binding energy collides with and ejects the inner electron creating an unstable vacancy.
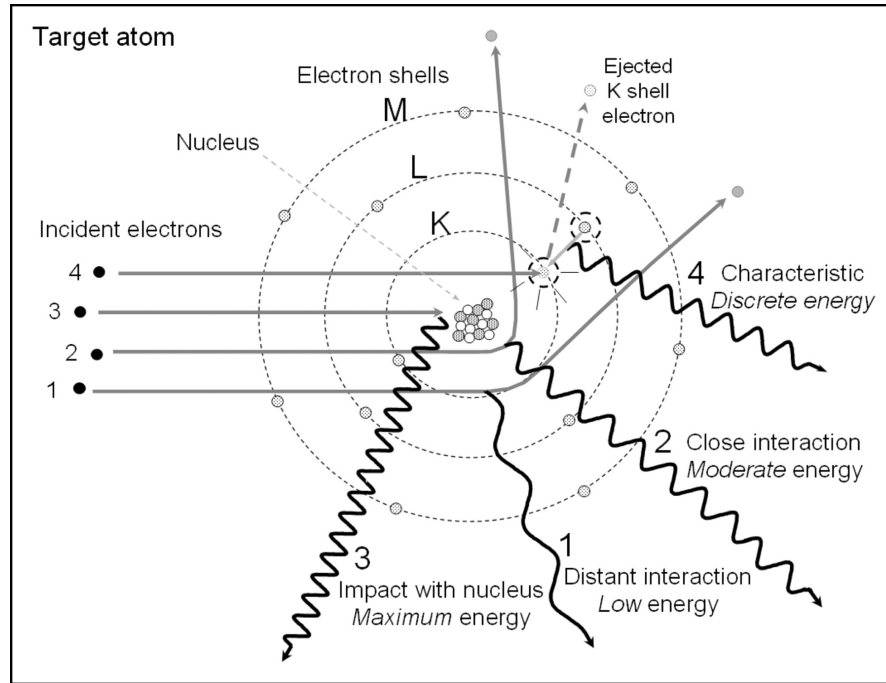
FIGURE 3.1: Bremsstrahlung production and of characteristic X-rays: the events 1, 2, and 3 depict incident electrons interacting in the vicinity of the target nucleus, resulting in bremsstrahlung production follow by the emission of a continuous energy spectrum of photons; event 4 demonstrates characteristic radiation emission, when an incident electron with energy greater than the K-shell binding energy collides with and ejects the inner electron creating an unstable vacancy [18].

The energy loss due to bremsstrahlung for high energies is given by:

$$-\frac{dE}{dx} = \frac{4\alpha N_A Z^2 z^2}{A} \left(\frac{e^2}{4\pi\varepsilon_0 mc^2}\right)^2 \cdot E \cdot ln\left(\frac{183}{Z^{1/3}}\right) \tag{3.3}$$

where $\alpha$ is the fine-structure constant of the electromagnetic interaction, $N_A$ is the Avogadro number, $Z$ is the atomic number of the traversed material, and $A$ is its mass number. $\varepsilon_0$ is the electric constant, while $z$, $m$, and $E$ are the charge, the mass, and the energy of the decelerated particle. The energy loss caused by bremsstrahlung is proportional to $E = m^2$. It was demonstrated that this effect dominates above the critical energy $E_{crit} \simeq 550 MeV/Z$, the energy where the losses due to ionization and bremsstrahlung for electrons are the same [19].

### 3.1.2 Cherenkov radiation

When highly radioactive objects are observed under water, such as in "swimming pool" reactors and in the underwater temporary spent fuel storage areas at nuclear reactors, they are seen to be bathed in an intense blue light called Cherenkov radiation.

In this case, the Cherenkov radiation is caused by particles entering the water at speeds greater than the speed of light in the water. As the particles slow down to the local speed of light, they produce a cone of light roughly analogous to the bow wave of a boat which is moving through water at a speed greater than the wave speed on the surface of the water.
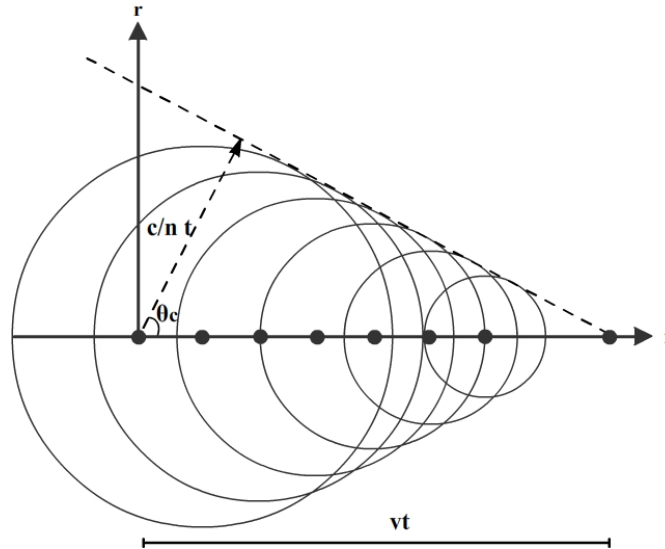


FIGURE 3.2: Construction of the Cherenkov emission angle via elementary waves emitted from each point of the trajectory adding up constructively along a line.

In general, Cherenkov radiation is emitted when charged particles pass through matter with a velocity $v$ exceeding the velocity of light in that medium. No particle can exceed the speed of light in a vacuum, but in materials with an index of refraction represented by $n$, the particle velocity $v$ will be greater than the velocity of light if $v > c/n$, that is, by particles for which $\beta > 1/n$. In this case a wave front will be formed in the medium.

Cherenkov radiation is emitted at polar angle $\theta_c$ with respect to the particle path:

$$cos(\theta_c) = \frac{1}{\beta n} \tag{3.4}$$

for $v > c/n$ and $cos(\theta_c) < 1$ if $\beta > 1/n$.

The mean number of photons produced by a particle with the charge $ez$ at a given wavelength $\lambda$ is [20]:

$$\frac{d^2N}{dxd\lambda} = \frac{2\pi\alpha z^2}{\lambda^2}\left(1 - \frac{1}{\beta^2 n^2(\lambda)}\right) \tag{3.5}$$

One of the valuable applications of Cherenkov radiation is the detection and identification of particles. Cherenkov counters utilize one or more of the properties of Cherenkov radiation:

- the existence of a threshold for Cherenkov radiation;

- the dependence of $\theta$ on the velocity $v = \beta c$ of the particle;

- the dependence of the number of emitted photons on the velocity of the particle.

### 3.1.3 Transition radiation

Transition radiation is a radiation in the X-ray region produced by relativistic charged particles when they cross the interface of two media of different dielectric constants $\varepsilon$ [21].

The energy of the emitted transition radiation photon is approximately proportional to the Lorentz factor, $\gamma = \frac{1}{\sqrt{1-\beta^2}}$, of the particle ($\gamma > 1000$) and because of this, the linear dependence on $\gamma$ of the transition radiation (TR) spectrum can be used to separate charged particles with similar momentum but different mass, like electrons and pions.

For ultra-relativistic particles crossing a boundary, the emitted radiation intensity $W$ depends on the frequency and the emission angle of the photon and is given by [22]:

$$\frac{d^2W}{d\omega d\theta} = \frac{2\alpha_e \hbar \theta^3}{\pi} \left( \frac{1}{1/\gamma^2 + \theta^2 + \omega_1^2/\omega^2} + \frac{1}{1/\gamma^2 + \theta^2 + \omega_2^2/\omega^2} \right)^2 \quad (3.6)$$

with $\theta$ as the emission angle of the transition radiation photon with respect to the particle trajectory, $\alpha_e$ is the fine-structure constant of the electromagnetic interaction, $\omega$ is the transition radiation photon frequency and $\omega_1$ and $\omega_2$ are the plasma frequencies of the traversed media. The plasma frequency is the self-oscillation of an electrically neutral medium, where the opposite electric charges are displaced. The charges perform a spatial oscillation. The frequency of this oscillation is the plasma frequency of the medium.

The differential energy spectrum is:

$$\frac{dW}{d\omega} = \frac{\alpha \hbar}{\pi} \left[ \left( \frac{\omega_1^2 + \omega_2^2 + 2\omega^2/\gamma^2}{\omega_1^2 - \omega_2^2} \right) \cdot ln \left( \frac{1/\gamma^2 + \omega_1^2/\omega^2}{1/\gamma^2 + \omega_2^2/\omega^2} \right) - 2 \right] \quad (3.7)$$

The total radiation intensity emitted at a single interface:

$$W = \frac{\alpha\hbar}{\pi} \cdot \frac{(\omega_1 - \omega_2)^2}{\omega_1 + \omega_2}\gamma \tag{3.8}$$

The angular distribution of transition radiation is peaked forward with a sharp maximum at $\theta = 1/\gamma$ [23].

If a charged particle is traversing a thin film with a width $L$, the transition radiation in the medium will be characterized by a wavelength $\lambda'$ and an emission angle of $\theta'$.

If $O$ is set as an observation point and $A$ and $B$ are the entrance and exit points, then the optical path difference to $O$ leads to a phase difference of $2\delta$ between waves produced at the entrance and exit point. An interference pattern can be observed due to the amplitudes $A$ and $-A$ with an optical path length difference equivalent to the phase difference $\delta$ from the perspective of point $O$. The intensity $I$ is given by [24]:

$$I = |A_A + A_B|^2 \simeq 4|A|^2 sin^2(\delta) \tag{3.9}$$

which, if $\delta \to \pi/2$, has a maximum for constructive interference and a minimum for destructive interference if, $\delta \to 0$. For a phase difference at the entrance and exit point of $180°$, a sufficient optical path length difference [24]:

$$\delta \sim \frac{\omega L}{4c} \left[ \left(\frac{\omega_p}{\omega}\right)^2 + \theta^2 + \frac{1}{\gamma^2} \right] \tag{3.10}$$

The double differential cross section for transition radiation is proportional to the fine structure constant $\alpha$ and is given by [24]:

$$\frac{d^2 N_{TR}}{d\omega d\Omega} \sim \frac{\alpha}{\pi^2\omega} \cdot \left[ ln\left(1 + \frac{1}{y^2}\right) \cdot \left(y^2 + \frac{1}{2}\right) - 1 \right] with y = \frac{\omega}{\gamma\omega_p} \tag{3.11}$$

where $\omega_p$ is the plasma frequency of the radiator material. The photon spectrum falls off rapidly for $y > 1$ or $\omega$ larger than $\gamma\omega_p$ being the characteristic frequency.

The total energy radiated from passing a single layer is found to depend on the squared difference of the plasma frequencies $\omega_p$ of the two materials; if the difference is large ($\hbar\omega_{air} \approx 0.7eV$ and $\hbar\omega_{polypropylene} \approx 20eV$) the relation is:

$$E \approx \frac{2}{3}\alpha\gamma\hbar\omega_p \tag{3.12}$$

where $\alpha = \frac{1}{137}$ with an average number of radiated photons of the order [23].

$$\langle N \rangle \approx \frac{\alpha \gamma \omega_p}{\hbar \langle \omega \rangle} \tag{3.13}$$

Because the number of produced photons per interface crossing is very small, about 1%, several hundred interfaces are used in practical transition radiation detectors.

## 3.2 Interaction of photons with matter

Photons are electromagnetic radiation with zero mass, zero charge, and a velocity that is always $c$, the speed of light. Because they are electrically neutral, they do not steadily lose energy via Coulomb interaction with atomic electrons as charged particles do. Instead they travel some considerable distance before undergoing an interaction.

Photon penetration in matter is governed statistically by the probability, per unit travelled distance, that a photon interacts by one physical process (interaction type) or another. This probability is called the linear attenuation coefficient, $\mu$, and has the dimensions of inverse length (e.g. cm$^{-1}$). The coefficient $\mu$ depends on photon energy and on the material being traversed. The mass attenuation coefficient $\mu/\rho$ is obtained by dividing $\mu$ by the density $\rho$ of the material. It is usually expressed in cm$^2$g$^{-1}$, and represents the probability of an interaction per gcm$^{-2}$ of material traversed.

The intensity $I$ of a photon beam in matter is given by: $I = I_0 e^{-\mu x}$, where $I_0$ represents the intensity without absorption and $\mu$ (mass attenuation coefficient) is related to the photon interaction cross section $\sigma_i$ by:

$$\mu = \frac{N_A}{A} \sum_{i=1}^{3} \sigma_i \tag{3.14}$$

### 3.2.1 Photoelectric effect

In the photoelectric absorption process, a photon undergoes an interaction with an absorber atom in which the photon completely disappears. In its place, an energetic electron is ejected from one of the bound shells of the atom. The interaction is with the atom as a whole and cannot take place with free electrons since conservation laws would be violated. For photons of sufficient energy, the most probable origin of the photoelectron is the most tightly bound or K shell of the atom. The photoelectron appears with an energy given by:

$$E_{e^-} = h\nu - E_b \tag{3.15}$$

where $E_b$ represents the binding energy of the photoelectron in its original shell. Thus for photon energies of more than a few hundred keV, the photoelectron carries off the majority of the original photon energy.

The interaction leaves an ionized absorber atom with a vacancy in one of its bound shells. This vacancy is quickly filled through the capture of a free electron from the medium and/or rearrangement of electrons from other shells of the atom. Therefore, one or more characteristic X-ray photons may also be generated. The excited ion can then return to its ground state mainly through two competing mechanisms: fluorescence and Auger effect.

The process is enhanced for absorber materials of high atomic number $Z$. The photoelectric interaction is most likely to occur if the energy of the incident photon is just greater than the binding energy of the electron with which it interacts. As a result, the plot of the attenuation coefficient as a function of the photon energy is a complicated relationship, with sharp peaks at the binding energies of the various orbital shells and with strong dependence on the atomic number of the atom. Fig.3.3 is a log-log plot of the photoelectron interaction probability versus energy.
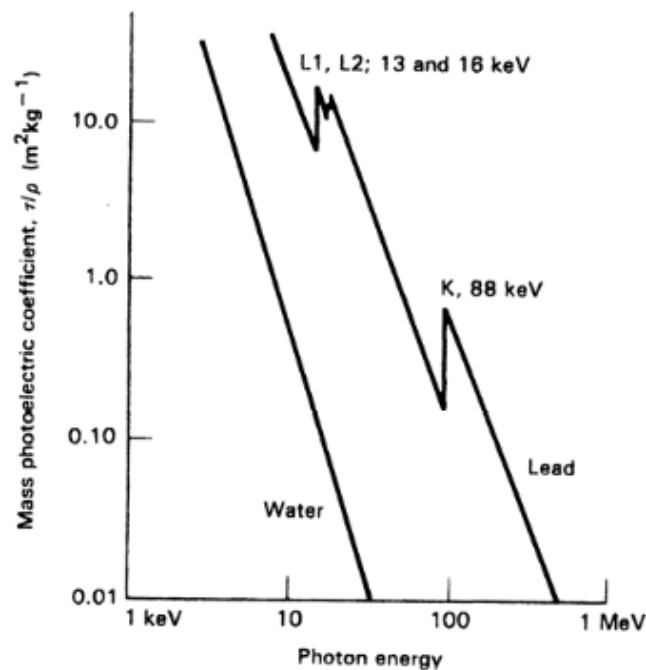


FIGURE 3.3: Photoelectric mass attenuation coefficient, plotted as a function of photon energy for water and for lead [25].

The K and L orbital edges for lead are visible. Since the K and L binding energies for water are so low, they are not visible in this plot.

### 3.2.2 Compton effect

The interaction between a photon with an electron is called Compton. Part of the energy of the photon is transferred to the scattering electron, which recoils and is ejected from its atom, and the rest of the energy is taken by the scattered, "degraded" photon. The result is a decrease in the photon energy (increase in wavelength), called the Compton effect.
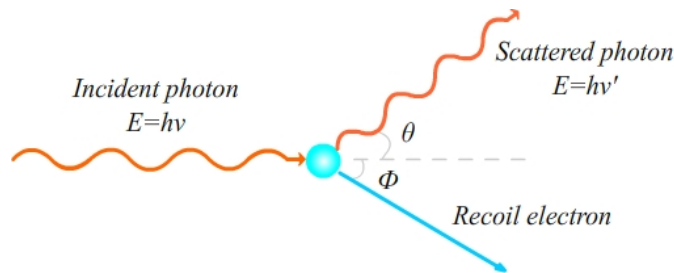


FIGURE 3.4: The Compton scattering of a photon.

In Compton scattering, the incoming photon is deflected through an angle $\theta$ with respect to its original direction. The photon transfers a portion of its energy to the electron (assumed to be initially at rest), which is then known as a recoil electron, or a Compton electron. Because all angles of scattering are possible, the energy transferred to the electron can vary from zero to a large fraction of the gamma-ray energy.

After the scattering with a free electron, the wavelength of the photon is increased by:

$$\Delta\lambda = \frac{h}{m_e c}(1 - cos\phi) \tag{3.16}$$

where $\phi$ is the angle by which the photon direction has changed due to the scattering. The frequency and energy of the photon reduce according to the wave length, whereas the energy of the electron increases by this amount. The maximum recoil energy of the electron allowed by kinematics is given by:

$$T_{max} = h\nu\left(\frac{2\gamma}{1+2\gamma}\right) \tag{3.17}$$

with $\gamma = \frac{h\nu}{m_e c^2}$.

### 3.2.3   Pair production

If an energetic photon enters matter and if it has an energy in excess of 1.02 MeV, it may interact by a process called pair production. In this mechanism of energy transfer, the photon, passing near the nucleus of an atom, is subjected to strong field effects from the nucleus and may disappear as a photon and reappear as a positive and negative electron pair without violating conservation of momentum. Since the momentum of the initial photon must be absorbed by something, pair production cannot occur in empty space out of a single photon; the nucleus (or another photon) is needed to conserve both momentum and energy.
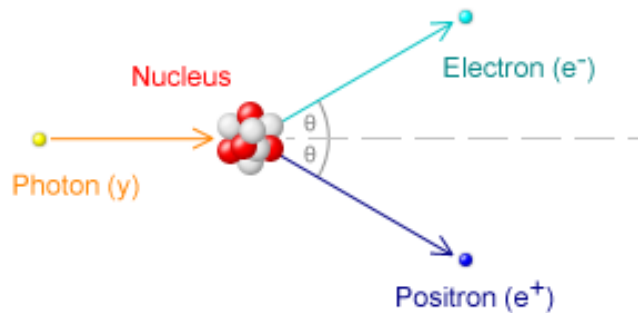
FIGURE 3.5: Pair production [26].

Pair production becomes more likely with increasing photon energy, and the probability increases with atomic number approximately as $Z^2$.

## 3.3   Basic operation of a Transition Radiation Detector

The Transition Radiation Detector (TRD) is used to discriminate between electrons and pions by a suppression factor of the order of 100 at an electron efficiency of 90% and for tracking of charged particles.

The principle of a transition radiation detector is based on the process presented in Chap.3.1.3. When a relativistic charged particle traverses the boundary of two media of different electric constant, it produces transition radiation (TR).

A transition radiation detector consists of two different main parts: a radiator, in which an electron creates the transition radiation, and a detection part consisting of a multiwire proportional chamber (MWPC) filled with a mixture of Xe (or Ar) and $CO_2$ in which the energy loss of charged particles and the TR photons can be measured.

The multiwire proportional chamber subsumes a large area drift chamber with the drift direction perpendicular to the wire planes, and a readout chamber.

A particle traversing a TRD module enters the drift chamber together with the produced transition radiation photon. Both the charged particle and associated photon ionize the gas in the chamber and create electron clusters. The transition radiation photon is absorbed shortly after entering the drift chamber due to the efficient TR-photon absorption provided by the chosen gas mixture.

The charged particle constantly produces a track of electron clusters on its way through the chamber. These electrons drift towards the amplification region where they are accelerated and further collide with gas atoms, thus producing avalanches of electrons around the anode wires; the operation principle can be followed in Fig.3.6.

The large cluster at the beginning of the drift chamber produced from the transition radiation photon is produced with higher probability by electrons than by pions, at the same moment, due to the large difference in their mass, and therefore used to identify electrons from the large pion background. The average pulse shape versus the drift time for electrons and pions is shown in Fig.3.7 [15], it can be seen that electrons and pions have different pulse heights due to the different ionization energy loss. A characteristic peak at larger drift times of the electrons is due to the absorbed transition radiation.

The produced electrons via energy loss due to ionization and transition radiation absorption will induce signals on the cathode pads.

### 3.3.1 Radiator material

As it was mentioned already, the transition radiation is produced when a highly relativistic charged particle (particles with $\gamma > 1000$) passes from one medium into another. As shown in Eq.3.8, the probability for the creation of a transition radiation photon from a single interface is only of the order of the fine structure constant $\alpha = 1/137$. A possibility to enhance the yield of radiated photons along a particle trajectory is to increase the number of crossed boundaries by using several hundreds of consecutive interfaces, a structure called radiator.

In principle there are three types of radiators: foil radiators, fiber radiators and foam radiators. A systematic study of these materials was done for the TRD of the ALICE experiment at LHC and the results can be found in [27].

These results showed that the most efficient radiators are the regular foil radiators. The disadvantage of these types of radiators is that they are very heavy and expensive because of the complex production procedure and has not yet been done for large areas as it is needed for the CBM experiment. Using foil radiators would require to mount hundreds of foils with uniform separation in strong metal frames.
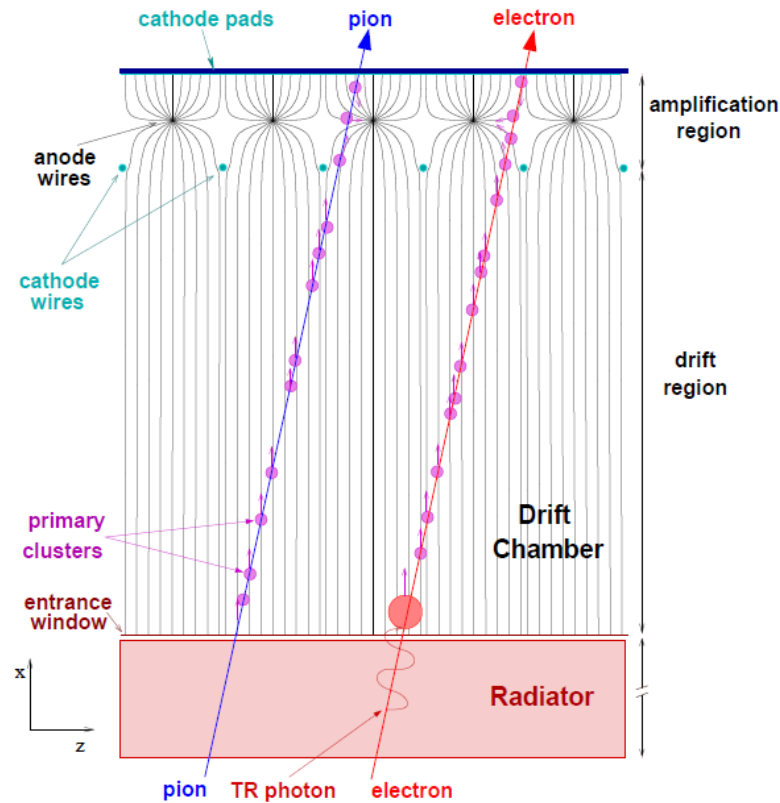
FIGURE 3.6: The TRD operation principle (projection in the plane perpendicular to the wires). Electrons produced by ionization energy loss and by TR absorption drift along the field lines toward the amplification region where they produce avalanches around the anode wires; these avalanches induce a signal on the cathode pads [27].
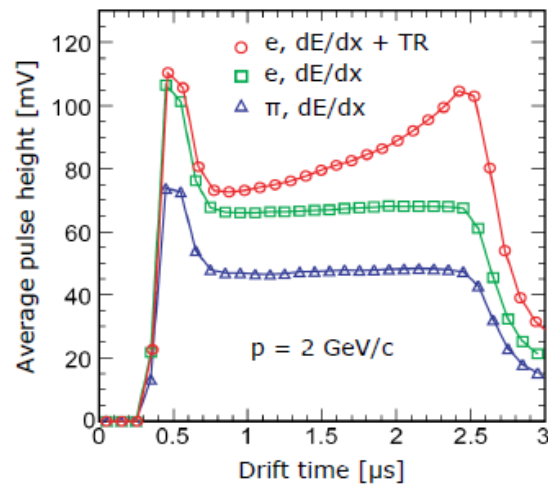


FIGURE 3.7: Average pulse height versus drift time. The different pulse heights indicate the different ionization energy loss of electrons (green rectangles) and pions (blue triangles). The characteristic peak at larger drift times of the electron (red circles) is due to the absorbed transition radiation [27].

In the case of TRD for the ALICE experiment, the solution was to use irregular radiators made of fibers. Such sandwich radiators, consisting of fiber mats sandwiched by two layers of foam, are used in order to provide the optimal combination of transition radiation efficiency, minimum weight and mechanical stability (a detailed description can be found in [27]).

The fiber mats, consisting of polypropylene fibers of 17 $\mu$m , which are predominately layered in two dimensions, are comparable in performance to regular foil radiators since the fiber thickness provides a well defined spatial separation between two consecutive boundaries, and a large fraction of the boundaries are approximately perpendicular to the particle flight direction.

The polymethacrylimide foam radiator, ROHACELL HF71, is a slightly less efficient radiator because of the random orientation of the boundaries and variably sized spatial gaps between them but offers very advantageous mechanical properties.

The TRD prototypes studied in this work were tested using a regular foil radiator, labelled Reg2 which has 220 foils of 20 $\mu$m thickness with a spacing of 250 $\mu$m, and irregular radiators (fiber, foam, sandwich), the results are presented in Chap.5.3.

### 3.3.2 Multiwire proportional chambers

Multiwire Proportional Chambers (MWPCs) are high-granularity fast detectors which allow track reconstruction of charged particles with good position resolution and the determination of their energy loss in the sensitive chamber volume.
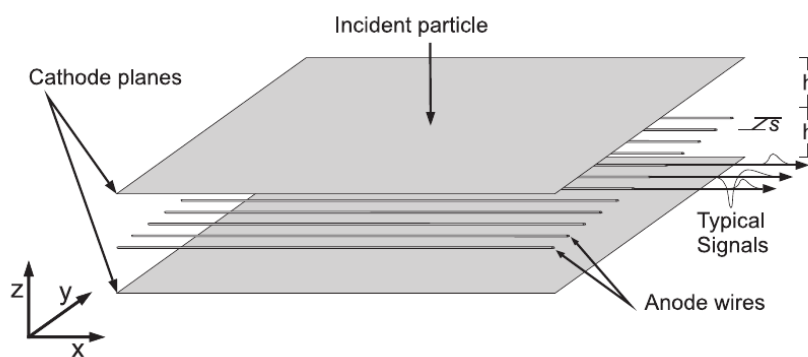


FIGURE 3.8: Sketch of a MWPC [23].

A multiwire proportional chamber consists essentially of a set of thin, parallel, and equally spaced anode wires, symmetrically sandwiched between two cathode planes (see Fig.3.8). In principle, each wire acts as an independent proportional counter. When

a negative potential is applied to the cathode planes, the anodes being grounded, an electric field develops which is approximately given by:

$$E(y, z) = \frac{CV_a}{2\varepsilon_0 s} \frac{\sqrt{1 + tan^2\left(\frac{\pi y}{s}\right) \cdot tanh^2\left(\frac{\pi z}{s}\right)}}{\sqrt{tan^2\left(\frac{\pi y}{s}\right) + tanh^2\left(\frac{\pi z}{s}\right)}} \tag{3.18}$$

where, $C$ is the capacity per length unit, $V_a$ is the applied anode voltage, the anode wire pitch $s$ and $r_a$ the anode wire radius:

$$C = \frac{2\pi\varepsilon_0}{\frac{\pi h}{s} - ln\left(\frac{2\pi r_a}{s}\right)} \tag{3.19}$$

In the region far away from the anode wires (20 times the wire-diameter), the field lines are essentially parallel and the field density is almost constant. Close to the anode wires, the field shows an $1/r$ dependence similar to a single wire cylindrical proportional chamber. The wire radii, 20 $\mu$m, are much smaller than the distance between the wires.

Far away from the anode wires, the electrons and ions liberated by an ionising process in a constant field region, drift along the field lines toward the nearest anode wire and opposing cathode. Near the high field region, the electrons are quickly accelerated and produce an avalanche. The electron avalanche is rapidly collected by the wires, the trailing positive ions move in opposite direction toward the cathode. In their motion, the electrons induce image charges in all surrounding electrodes.

The cathode signal is read-out, and the coordinate of the induced charge can be obtained by a subdivision of the cathode into readout pads perpendicular to the anode wires.

In order to obtain the best possible position resolution in the cartesian coordinate system of the cathode pad plane the induced charge distribution should be shared between two or three adjacent pads. The signal to noise ratio decreases if the charge signal is shared by more than three pads. When the induced charge is measured only by one pad the position resolution is given by the pad width $W$.

Additionally to the cluster position reconstruction performance, MWPCs feature electron-pion separation by the additional TR photon signal generated by the electrons with identical momenta due to their lower mass compared to the pion mass, as it was mentioned above.

### 3.3.3 Gas mixture

The filling gas for proportional counters has to meet different requirements: low working voltage, high gain, proportional behaviour, and high rate capability. For a minimum working voltage, noble gases are usually chosen due to the lowest electric field intensities necessary for avalanche formation.

Excited noble gas atoms formed in the avalanche de-excite giving rise to high-energy photons capable of ionizing the cathode and causing further avalanches. This process can be minimized by the addition of a quencher such as $CO_2$. The quencher molecules absorb the radiated photons and dissipate this energy through dissociation or elastic collisions.

Because Ar is the most prevalent noble gas in the atmosphere it is the cheapest solution for filling multiwire proportional chambers and therefore the most commonly used in laboratory tests, but in order to maximize the absorption of transition radiation produced by the radiator, the gas mixture used in real experiments is based on Xe, because of its higher atomic number (Z = 54 in comparison to Z=18 for Ar) [23].

For the TRD prototypes which are studied in the present work the used gas mixture was 80%Xe (or Ar) and 20%$CO_2$.

# Chapter 4

# High granularity single sided TRD prototypes

For the planned Compressed Baryonic Matter (CBM) experiment, the Bucharest group has constructed and tested several CBM-TRD prototypes of which the last three, two identical small prototypes (labelled through this work as TRD1 and TRD2) and a real size prototype (TRD3), will be described in this thesis.

Like their predecessor [28], these three prototypes are designed to overcome the limitations regarding the signal rooting topology which characterizes the double-sided architecture [29] by implementing an architecture based on a multiwire proportional chamber coupled with a drift zone. Unlike their predecessor, these prototypes are designed to fulfil the high counting rate and high multiplicity requirements specific to the regions of low polar angles in the CBM-TRD subsystem.

The chamber design concept is retained from the previous small prototype [28]: a 2 x 4 mm amplification region and a 4 mm drift zone identical with the 4 x 3 mm double-sided prototype [29], an anode wire pitch of 3 mm and a cathode wire pitch of 1.5 mm. The drift size was chosen such to minimize the drift time ($< 250$ ns for 80%Xe-20%$CO_2$ gas mixture, 2000 V anode voltage and 500 V drift voltage [30]), while keeping the transition radiation conversion efficiency as large as possible.

## 4.1 2011 TRD small prototypes

Fig.4.1 shows the chamber's configuration of the TRD small prototype architecture. The multiwire chamber is closed on one side by the drift electrode made from a Rohacell plate of 8 mm thickness coated on the inner side by an aluminized kapton foil of 20 $\mu$m

thickness, and on the other side by the read-out electrode made from a 300 $\mu$m thickness PCB. In the middle of the amplification region lies the anode wire plane, made from Au coated W wires of 20 $\mu$m diameter; the amplification region is separated from the drift region by the cathode wire plane made from 70 $\mu$m diameter Cu-Be alloy.
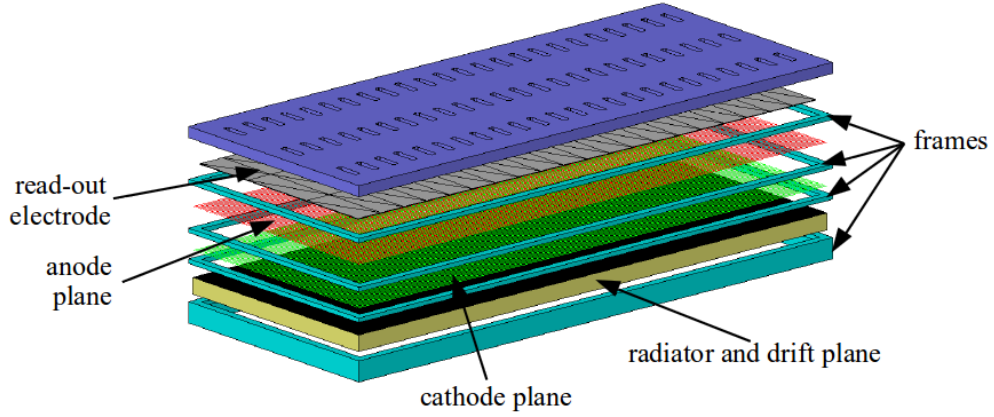


FIGURE 4.1: Sketch of the chamber configuration for the 2011 TRD prototype [31].

The read-out electrode, sketched in Fig.4.2, has a structure of three rows with 64 triangular pads per row. The triangular shape of the read-out pad gives access to the position information in both coordinates (more details in Chap.5.4) which defines the read-out electrode plane. The area of a read-out cell is $\sim$ 1cm$^2$ (2.7 cm height x 0.7 cm width) and corresponds to the requirements of the innermost zone of the first TRD station (as described in Chap.2.2). As it can be seen in Fig.4.2, the read-out electrode was equipped with two types of connectors: a first type (right side of Fig.4.2) that can be read-out by the 8 channel FASP front-end electronics [32] and a second type (left side of Fig.4.2) that can be operated by a 32 channel SPADIC [33] front-end electronics.
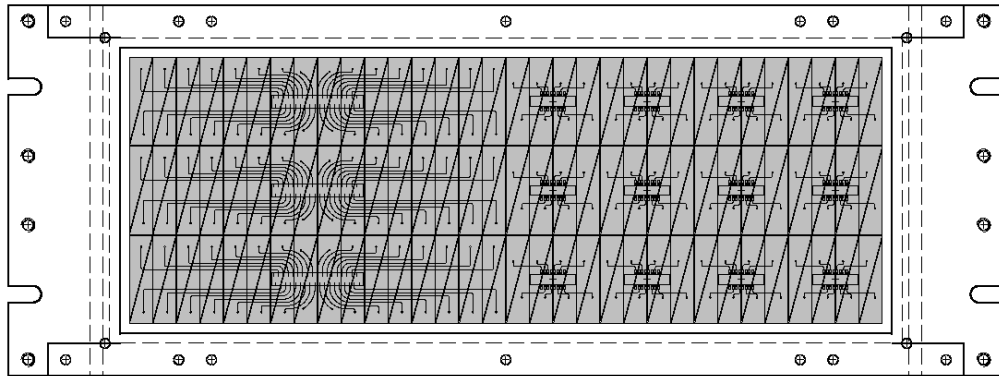


FIGURE 4.2: Sketch of the read-out electrode structure for the 2011 small size TRD prototype [34].

Two identical chambers were tested with a mixed beam of electrons and pions at CERN and the results of the measurements are presented in Chap.5.2.

## 4.2 2012 TRD real size prototype

The last version [35] of the single-sided TRD prototype [28] is a real size CBM-TRD prototype (539.8 x 557.8 mm$^2$) that was build and tested last year, in 2012.

The only difference (as it can be observed in Table 4.1) between the small prototypes and this one, with the exception of the size, is the structure of the drift electrode which is made from a 9 mm thick honeycomb plate placed between two Rohacell plates of 3 mm thickness, each one coated on the outer side with an aluminized kapton foil of 20 $\mu$m thickness. One side of the gaseous chamber is closed by the drift electrode, the other side is closed by the read out electrode made from a 300 $\mu$m thick PCB reinforced by a 2 cm thick honeycomb plate sandwiched by two layers of 100 $\mu$m carbon fiber.

The bottom sketch in Fig.5.27 shows a sketch of the read-out electrode of the real size TRD prototype and it's dimensions. It has a structure of *9 columns and* 20 triangular pad rows with 144 triangular pads per row, each triangular pad of $\sim 1$ cm$^2$ area, is readout individually.
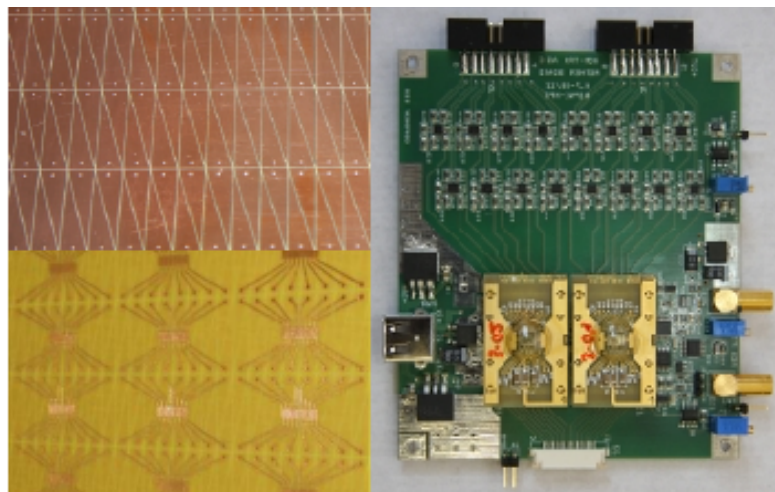


FIGURE 4.3: The read-out electrode (left side - up), the signal transport topology (left side - down) and the associated 16 channel FEE based on two FASP chips (right side).

Signals delivered by pads are routed in groups of 16 (left side - Fig.4.3) to the flat cables and processed by FASP front-end electronics (right side - Fig.4.3).

This real size TRD prototype was tested, in the laboratory, with a 5.9 keV X-ray $^{55}$Fe source and with a mixed beam of electrons and pions at CERN. The results of these tests are presented in Chap.5.

| Prototype / Feature | TRD2011 - small prototype | TRD2012 - real size prototype |
|---|---|---|
| **Architecture** | single MWPC (2 x 4 mm amplification region) + 4 mm drift region ||
| **Anode – Cathode gap** | 4 mm ||
| **Anode plane** | 20 $\mu$m gold plated W wires, 3 mm wire pitch ||
| **Cathode plane** | 70 $\mu$m Cu-Be wires, 1.5 mm wire pitch ||
| **Drift electrode** | 8mm Rohacell plate + 20 $\mu$m Al kapton foil | 20 $\mu$m Al kapton foil + 3 mm Rohacell + 9 mm honeycomb + 3 mm Rohacell + 20$\mu$m Al kapton foil |
| **Read-out electrode** | 192 triangular pads | 2880 triangular pads |
| | read-out cell area $\sim$ 1cm$^2$ (2.7 cm height x 0.7 cm width) ||
| | total area of 8 x 29 cm$^2$ | total area of 539.8 x 557.8 mm$^2$ |

TABLE 4.1: Design details of TRD prototypes.

# Chapter 5

# Performance of TRD prototypes

## 5.1 $^{55}$Fe source measurements

### 5.1.1 Data calibration and energy resolution

The real size TRD prototype was tested in detail in the detector laboratory of the Hadron Physics Department of IFIN-HH using a collimated $^{55}$Fe radioactive source, $\Phi$=1 mm. The $^{55}$Fe source emits X-ray of 5.9 keV and the photons were absorbed by the detection gas mixture of Ar and $CO_2$ (80%-20%).

The source was carefully collimated onto the center of a rectangular pad as it can be seen in Fig.5.2 where the charge on three adjacent pads is represented. The plotted signals are corrected considering the electronics systematics from Fig.5.6, Fig.5.7 and Fig.5.8. The detector was operated at a drift high voltage of 800 V and several values for the anode high voltage: 1800 V, 1850 V, 1900 V, 1950 V, 2000 V and 2025 V.

During the measurements, the signals from 24 rectangular pads (hardware paired triangular pads), 8 pads per row, were read-out. The signals were processed using a Fast Analog Signal Processor v0.1 (FASP-0.1 [32]) also developed by the Bucharest group. The ASIC chip was designed in AMS CMOS 0:35 $\mu$m technology. Its main characteristics are a selectable shaping time of 20 ns or 40 ns and a 6.2 mV/fC conversion gain. For a 25 pF input capacitance, the equivalent noise charge is less than 980 electrons for 40 ns shaping time and less than 1170 electrons for 20 ns shaping time. The power consumption of the chip is about 11 mW/channel.

This version of FASP has 8 input channels and two types of outputs for each input channel: a fast output with a semi-Gaussian shape and a peak-sensing output (called "flat top") (see Fig.5.1). During the tests the flat top output was used, the shaping time
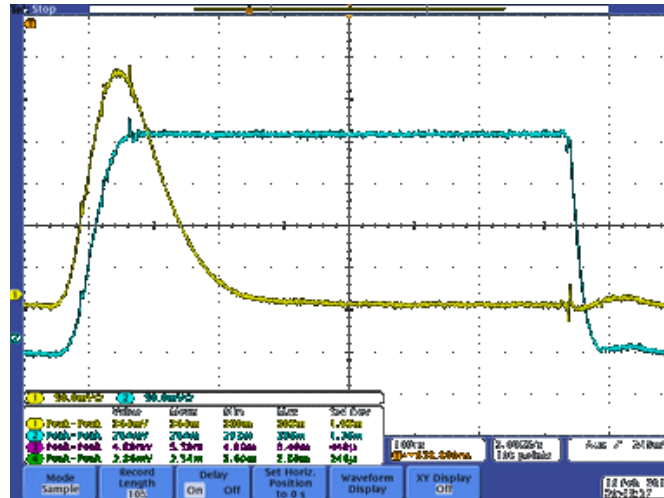
34

FIGURE 5.1: Fast output (yellow line) and flat top output (blue line) of the Fast Analogue Signal Processor.

was set at 40 ns and the analogue signals were digitized by a 32 channel peak sensing MESYTEC analogue to digital converter.
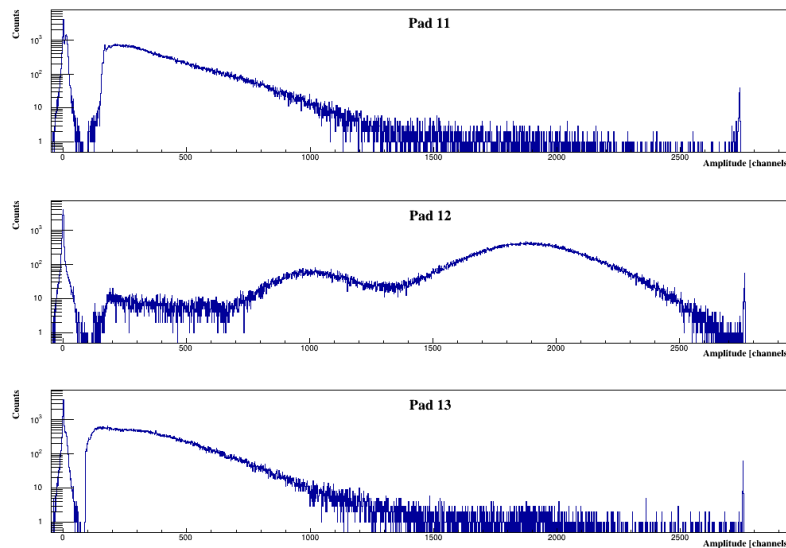


FIGURE 5.2: Calibrated charge on three adjacent pads. It is clear that the $^{55}$Fe source was collimated on pad 12 (the forth pad on the second row), pads 11 and 13 have almost the same charge, thus the positioning of the source on the center of a rectangular pad was achieved. The detector was operated at $HV_a = 2025\ V$ and $HV_d = 800\ V$.

Fig.5.6, Fig.5.7 and Fig.5.8 present the electronics systematics taken into consideration for data calibration. This systematic study is done for each motherboard and it refers at at the following characteristics:

- electronic pedestal

- gain per channel

- signal thresholds

### Electronic pedestal

Measurements without a detector response are conducted, the acquisition trigger is provided by a generator. The acquired information (see Fig.5.3) is thus the electronics pedestal. Each pedestal is fitted with a Gaussian function and the obtained mean values are retained as pedestal positions (Fig.5.6) and further considered in data calibration.
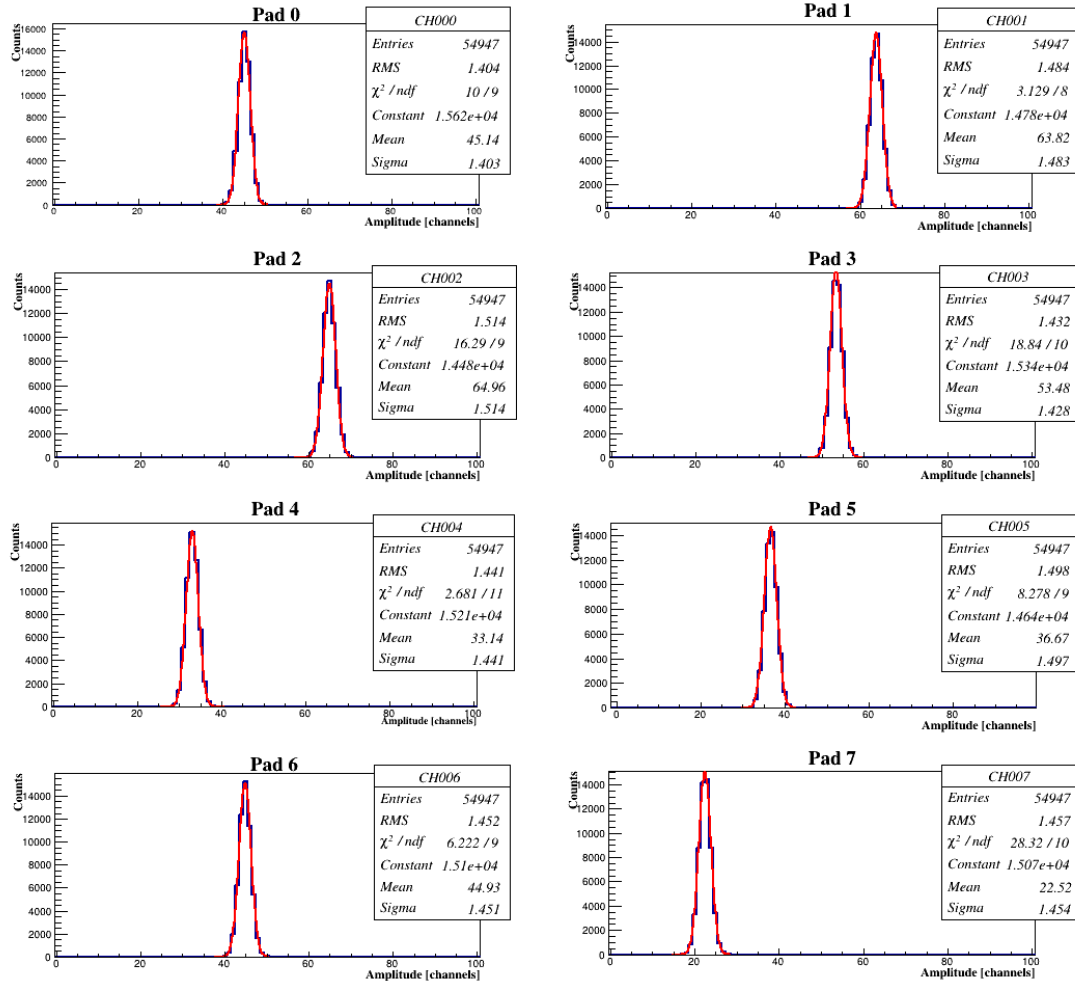


FIGURE 5.3: A pedestal run for 8 pads. The obtained spectra for each pad is fitted with a Gaussian function and the mean of the fit represents the position of the pedestal which is considered in the calibration algorithm.

### Gain per channel

Next step is the gain correction for each channel. This time a charge is injected on each pad from a pulser. The position of the converted signal in ADC channels obtained at five different values for the injected signal plotted as a function of the corresponding voltage values of the injected signal is represented in Fig.5.4 for eight pads. The gain characteristic for each pad is plotted in Fig.5.7.
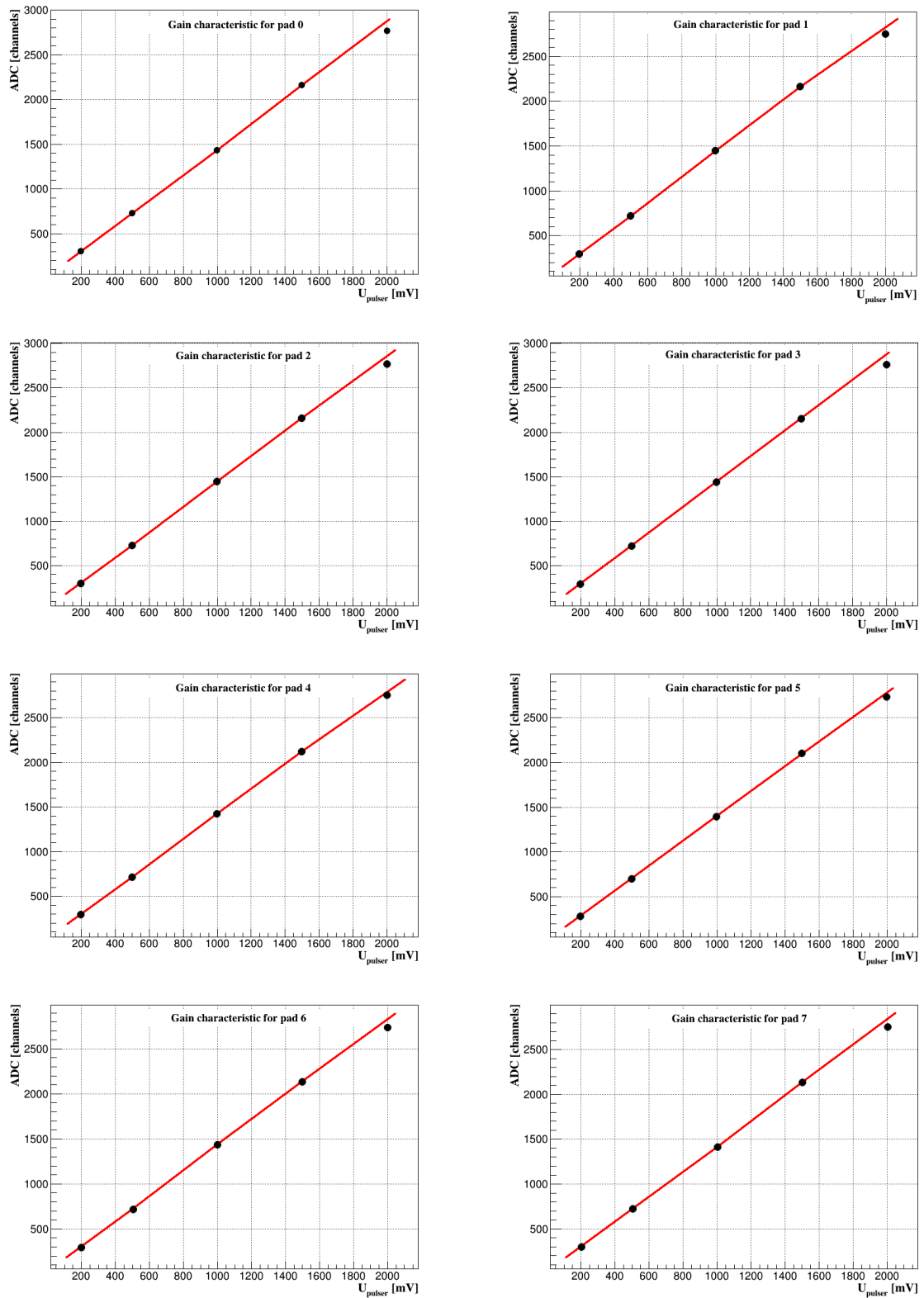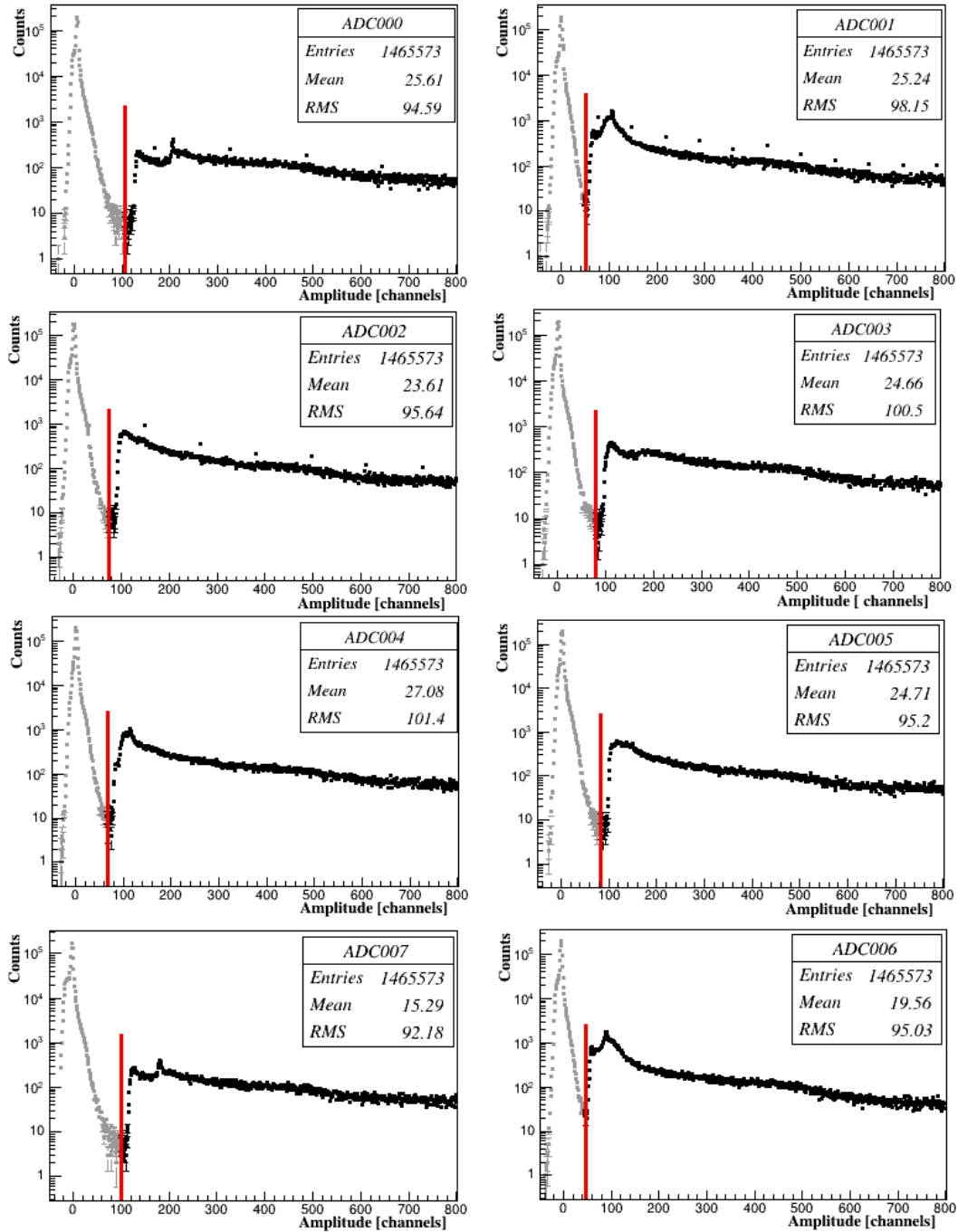
FIGURE 5.4: Gain characteristic for 8 pads.

FIGURE 5.5: A threshold run for one of the motherboards. The detector's surface was uniformly illuminated with the $^{55}$Fe source. The signal is represented in black, the noise is in grey.
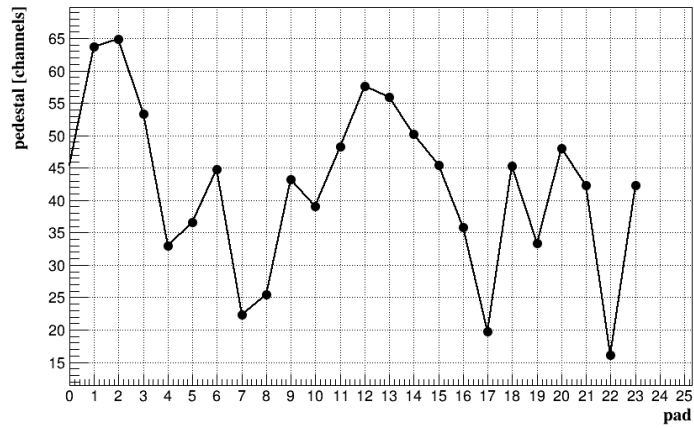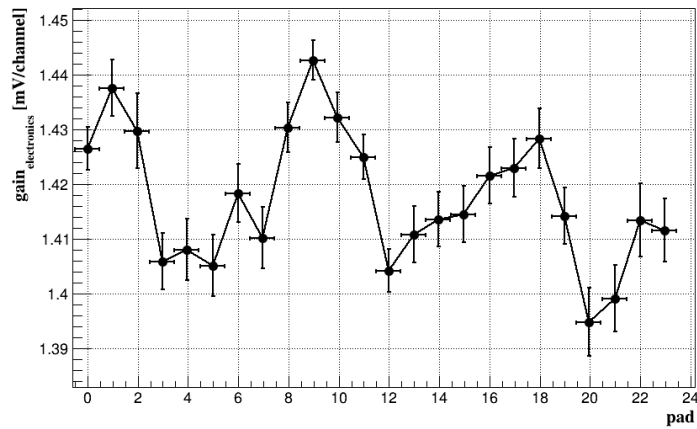
FIGURE 5.6: Channel pedestal systematics.
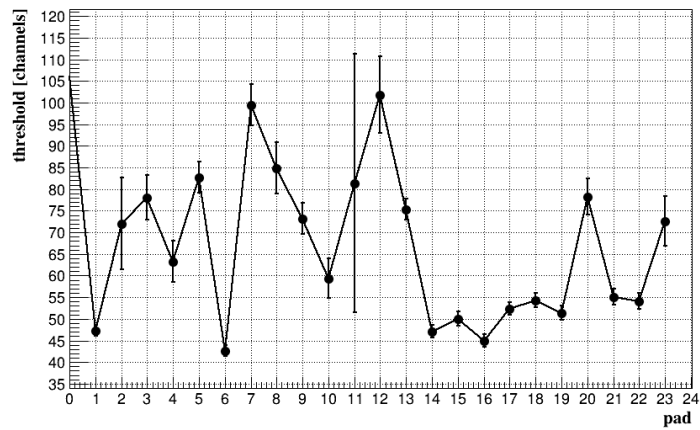


FIGURE 5.7: Channel gain systematics.



FIGURE 5.8: Channel threshold systematics.

**Signal threshold**

After the pedestal and gain corrections have been implemented, the detector's surface is uniformly illuminated with the X-ray source. The spectra on eight pads are presented in Fig.5.5 where the red line denotes the value of the threshold, the region represented in grey before this value is considered to correspond to the noise and the region, plotted in black, after this threshold value is considered to correspond to the the real signal. Fig.5.8 shows the threshold systematics for all 24 pads that were read-out during these experiments.

**Energy resolution and cluster size**

After the characterization of each motherboard the data from the measurements with the X-ray $^{55}$Fe source is corrected and the energy resolution of the detector can be determined.

Typical energy spectra obtained in $^{55}$Fe source tests and the energy resolution,in sigma, are shown in Fig.5.9 for different values of the applied anode voltage. An energy resolution of 8.196±0.011%, was obtained for the applied voltage of $HV_a = 2025V$ and $HV_d = 800V$.
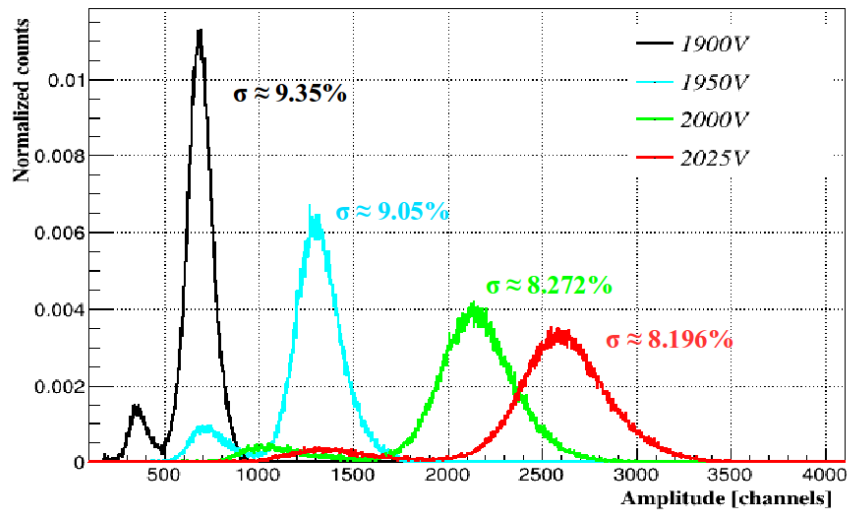


FIGURE 5.9: Energy resolution as a function of applied anode high voltage.

As explained in Chap.5.4.2 the signal can be shared between two or three adjacent pads. One way of increasing the degree of charge sharing is to rise de applied anode voltage as can be seen in Fig.5.10. The top plot shows the number of pads per cluster for all six values of the applied anode voltages. At low values for the anode voltage, 1800 V and 1850 V, there is no charge sharing between three adjacent pads. The

percentage of 3-pad clusters (Fig.5.10 - bottom plot) rises with increasing anode voltage, at $HV_a = 2025\ V$ a value of $\sim 91\%$ of events fire 3-pad clusters.
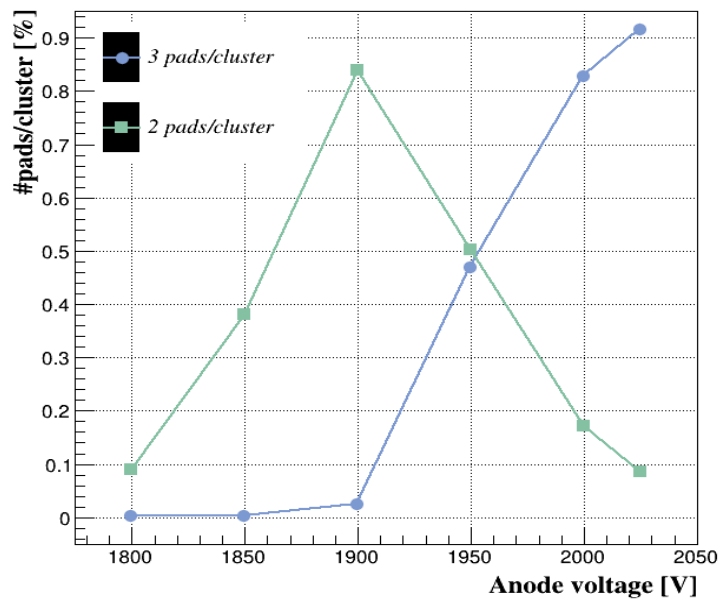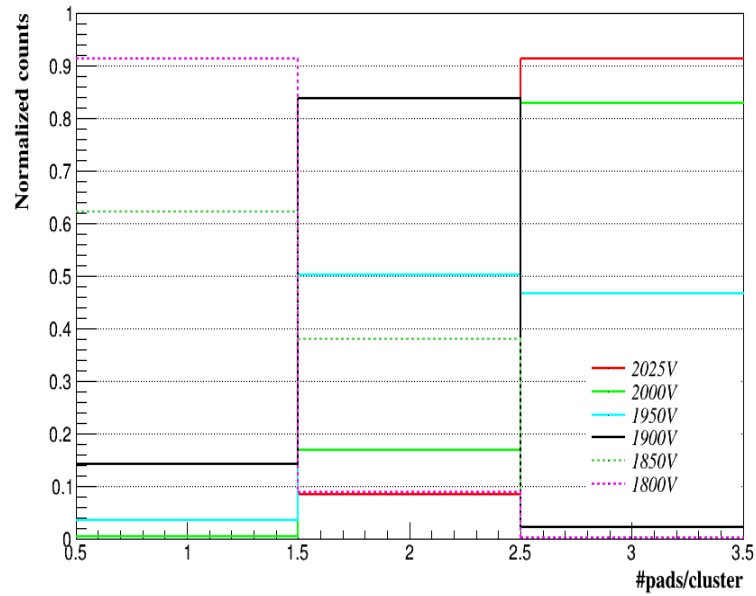


FIGURE 5.10: Cluster size as a function of anode voltage (top plot); the percentage of 3-pad clusters and 2-pad clusters as a function of applied anode voltage (bottom plot).
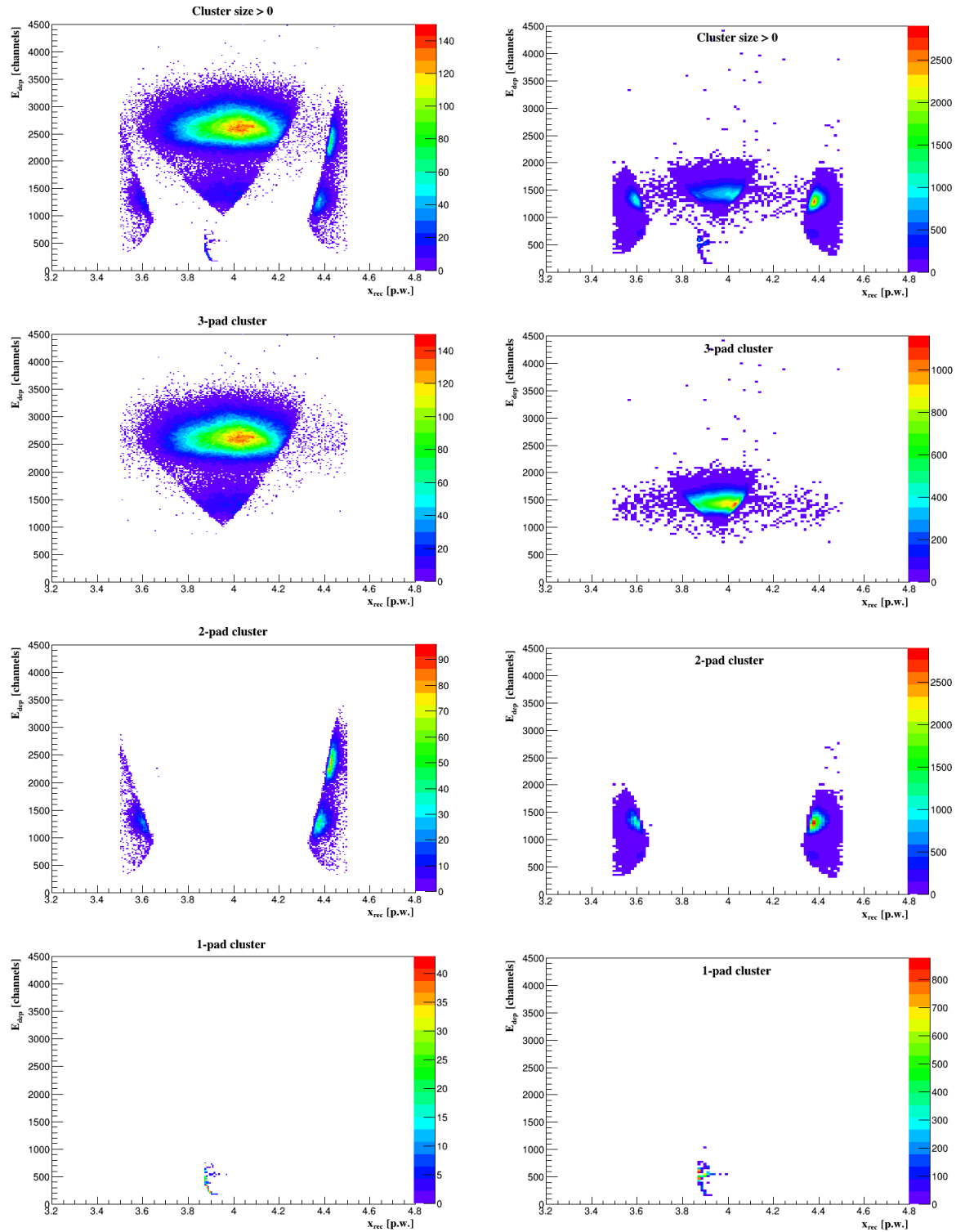
FIGURE 5.11: Deposited charge as a function of reconstructed position and as a function of cluster size. The detector was operated at an anode voltage of 2025 V (left-side plots) and 1950 V (right-side plots).

Fig.5.11 shows a representation of the deposited energy in the detector, $E_{dep}$, as a function of the reconstructed collimator position, $x_{rec}$, for two values of the applied high anode voltages: 1950 V (right side plots) and 2025 V (left side plots). For each case, the top pictures show the reconstructed position irrespective of the number of pads per cluster, while the next three pictures show how the cluster size influences the position reconstruction: 3-pad clusters lead to a position reconstruction in the center of the rectangular pad, while the 2-pad clusters are reconstructed on the edges of the pad.

### 5.1.2 Absorption measurements

Another set of tests were conducted in order to quantitatively characterize the absorption of different support structures of the drift electrode (detector's entrance). For this, 5 samples of different structures were tested using the collimated $^{55}$Fe source and the real size TRD prototype which was flushed with a gas mixture of Ar(80%) and $CO_2$(20%), and operated at $HV_a = 1900V$ and $HV_d = 600V$. The signals were collected directly from the anode.
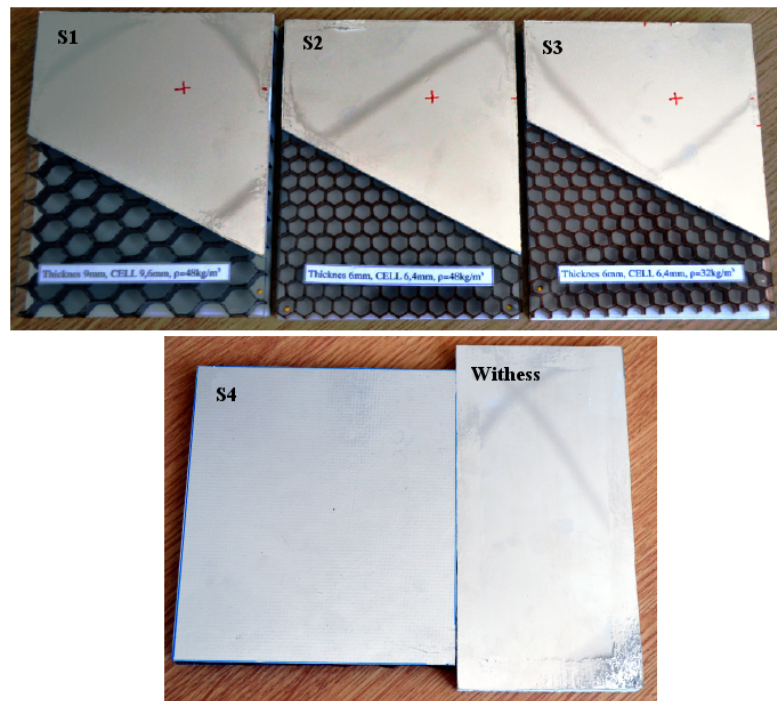


FIGURE 5.12: Tested samples.

The first three samples from Fig.5.12, labelled $S_1$, $S_2$ and $S_3$ have a sandwich like structure, composed from a honeycomb plate placed between two Rohacell plates, each one coated on the outer side with an aluminized Kapton foil (the structure is presented in Fig.5.12 and the characteristics of each sample are described in Table 5.1).

| Characteristic | $S_1$ | $S_2$ | $S_3$ | $S_4$ | Witness |
|---|---|---|---|---|---|
| **Rohacell thickness [mm]** | 2 x 3 | 2 x 3 | 2 x 3 | - | 8 |
| **Honeycomb thickness [mm]** | 9 | 6 | 6 | 9 | - |
| $\phi_{\mathbf{honeycombcell}}$ | 9.6 | 6.4 | 6.4 | 9.6 | - |
| **Honeycomb density $[kg/m^3]$** | 48 | 48 | 32 | 48 | - |
| **Al Kapton thickness $[\mu m]$** | 2 x 20 | 2 x 20 | 2 x 20 | - | 20 |
| **Absorption [%]** | 56.23 | 56.75 | 55.03 | 48.12 | 58.20 |

TABLE 5.1: Sample characteristics.

The forth sample, $S_4$ also has a sandwich structure: a honeycomb plate covered on both sides with an aluminized carbon foil of $\sim 300\ \mu$m.

The last sample, labelled *Witness* is a Rohacell plate of 8 mm thickness, coated only on one side with an aluminized Kapton foil (see Fig.5.12).

The results show (see Table 5.1) that the main absorber is, as expected, the Rohacell plate, the honeycomb contribution being negligible, irrespective of the sample.

The absorption for sample $S_4$, aliminized carbon foil and honeycomb plate, is of 48% compared to the witness, the 9 mm thick Rohacell plate, with an absorption of 58%. Also, sample $S_4$ has a transmission $\sim 25\%$ better than the witness sample, and $\sim 10\%$ better than the samples with a honeycomb structure.

## 5.2  In-beam tests at PS CERN

The transition radiation prototypes were tested with a mixed beam of electrons and pions made available at T9 beam line by CERN Proton Synchrotron during two beam time periods. The 5.13 and 5.14 pictures show the experimental set-up for the two beam tests conducted in 2011 and 2012.

A common CBM beam test setup consists of a Cherenkov detector and a lead-glass calorimeter between which a RICH prototype, a number of transition radiation detector prototypes from different research groups and the TOF RPC prototypes are aligned.

The tests consisted in operating the prototypes with variating parameters like the particle momenta (from 2 GeV/c up to 8 GeV/c), the applied anode and drift voltages and the type of radiator placed in front of the TRD prototypes. All operating conditions are presented for both beam periods in Table 5.2.

The signals provided by the read-out channels were processed by the new front-end electronics (FEE) the ASIC chip Fast Analog Signal Processor V0.1 (FASP-0.1 [32]).

| | Beam time 2011 | Beam time 2012 |
|---|---|---|
| **Beam conditions** | mixed beam of electrons and pions | |
| | particle momenta 2-10GeV/c | particle momenta 2-8GeV/c |
| **Prototypes tested** | 2 small TRD prototypes | 2 small TRD prototypes and a real size TRD prototype |
| **FEE** | FASP-VO.1 with peak sense output signal and a 40ns shaping time | |
| **Signal digitization** | 32 channel Mesytec ADC read-out | |
| **DAQ** | Multi-Branch System | |
| **Operation conditions** — types of radiators | regular foils, fibers, foam, pokalone, etc. | |
| **Operation conditions** — high voltage | $HV_a$=1800V-2100V $HV_d$=400V-800V | $HV_a$=2000V-2100V $HV_a$=800V |
| **Operation conditions** — gas mixture | Ar+$CO_2$ (80%+20%) Xe+$CO_2$ (80%+20%) | Xe+$CO_2$ (80%+20%) |
| **Signals read-out from** | individual triangular pads | |
| | rectangular pads=hardware paired triangular pads | |

TABLE 5.2: Beam and detector operation conditions for both beam time periods.

The shaping time set for the peak sense output signal of FASP was of 40 ns and the analogue signals were digitized by a 32 channel MESYTEC converter.
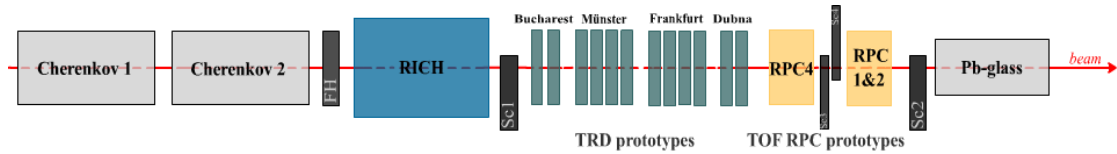


FIGURE 5.13: Experimental set-up @ CERN in 2011: The RICH prototype is followed by 12 different TRD prototypes from 4 laboratories: 2 from Bucharest, 4 from Muenster, 4 from Frankfurt and 2 from Dubna and by two RPC prototypes between which two scintillators were placed. In addition to the mentioned subsystems the set-up consisted of a fiber hodoscope and two beam trigger scintillators.
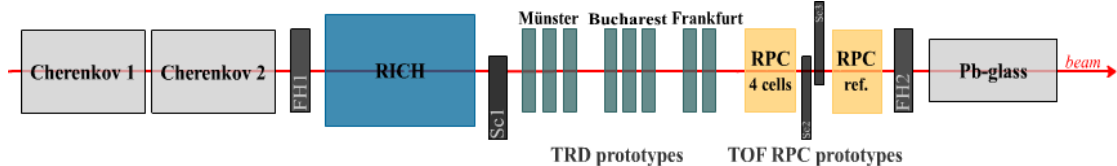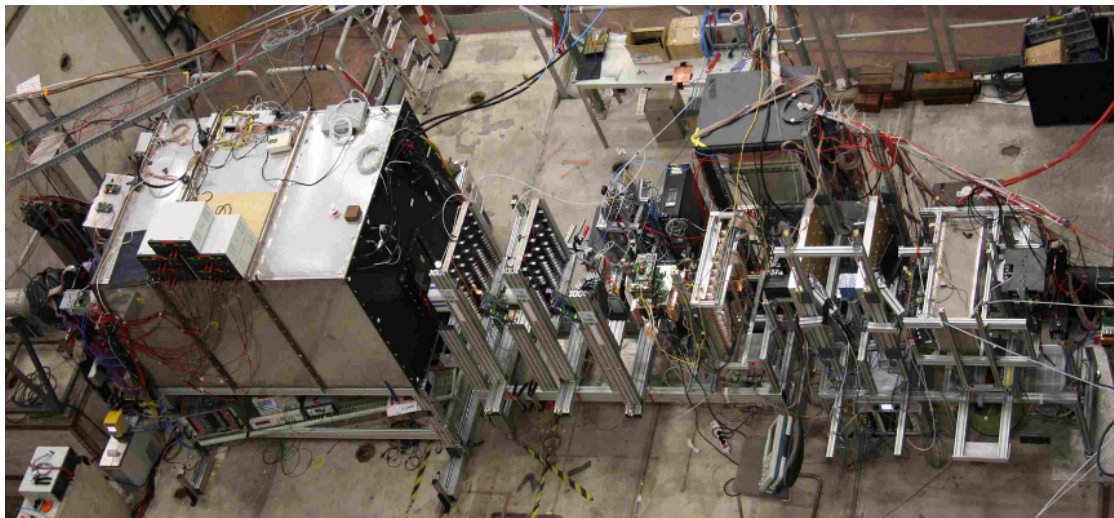


FIGURE 5.14: Experimental set-up @ CERN in 2012: As in the previous experiment, after the RICH prototype, and between the Cherenkov detector and lead-glass calorimeter, the TRD and TOF RPC prototypes were aligned, this time, the three Bucharest TRD prototypes were placed between the ones from Muenster and Frankfurt. Plastic scintillators provided the beam trigger.

## 5.3    Electron-pion identification

One of the functions of the transition radiation subsystem within the CBM experiment will be to identify highly energetic electrons and positrons (with a Lorentz factor $\gamma > 1000$) with a pion rejection factor of 1% at an electron efficiency of 90%.

Identification of charged particles like electrons and pions is done by measuring the lost energy due to ionization processes and, in addition for electrons, the transition
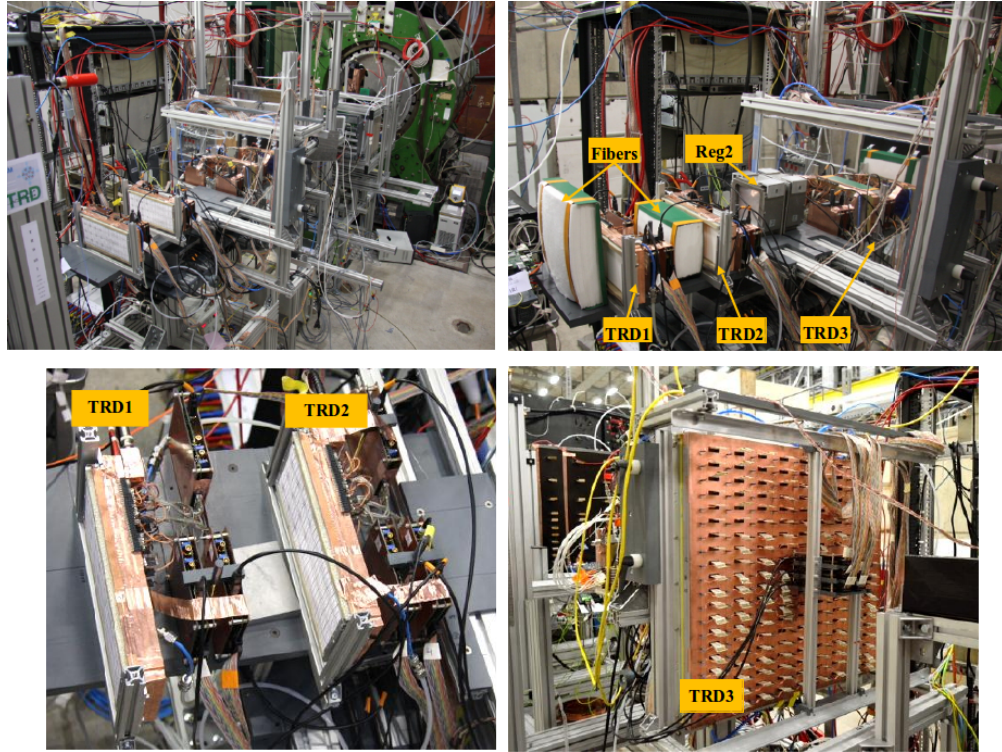
FIGURE 5.15: Close-up view of the experimental arrangement from CERN in 2012.

radiation. As was already presented in Chap.3.1.3, transition radiation (TR) is emitted when a charged particle crosses the boundary between two media with different dielectric constants [22]. More than one TR photons, typically soft X-rays, are produced if the Lorentz factor $\gamma$ of the charged particle is larger than about 1000. This Lorentz factor corresponds to electron momentum of about 0.5 GeV/c and pion momentum of about 140 GeV/c. Therefore detecting transition radiation can be used to identify electrons effectively in the momentum region from 0.5 GeV/c up to 140 GeV/c.

Samples of electrons and pions are selected using coincident cuts, as it can be seen in Fig.5.16, on signals delivered by a Cherenkov detector and a lead-glass calorimeter.

Fig.5.17 shows the distributions of the integrated charge (the sum on three adjacent readout pads $Q_i$, $Q_{i-1}$, $Q_{i+1}$) of the total energy deposit in the 2011 TRD prototype. In Fig.5.17 electrons (blue) and pions (red) samples, with particle momenta from 2 to 8 GeV/c, were identified using the Cherenkov and the Pb-glass detectors. The prototype was operated at $HV_a = 2000V$ and $HV_d = 800V$, in front of the detector entrance a regular foil radiator (Reg2) was placed and trough the chamber a gas mixture of Xe and $CO_2$ was flushed.

Due to the dE/dx relativistic rise, the separation between the pions and the electrons based only on $dE/dx$ would be reduced as function of momentum. That is why the TR
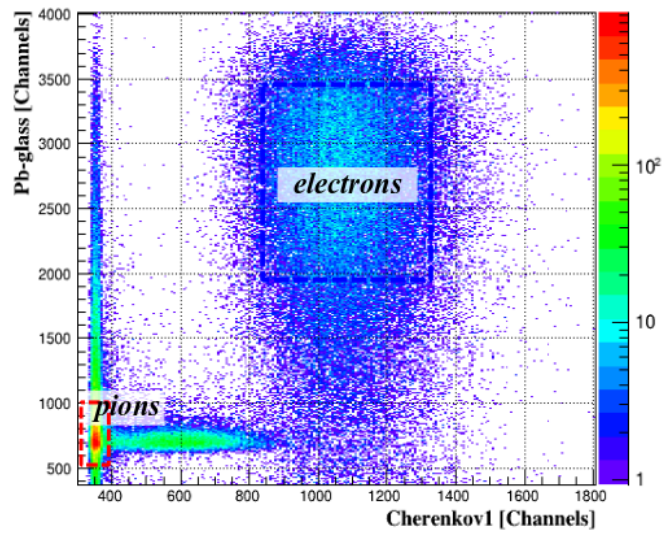
FIGURE 5.16: Cherenkov-Pb-glass correlation and the cuts used to identify pions and electrons plotted for particle momenta of 4 GeV/c.
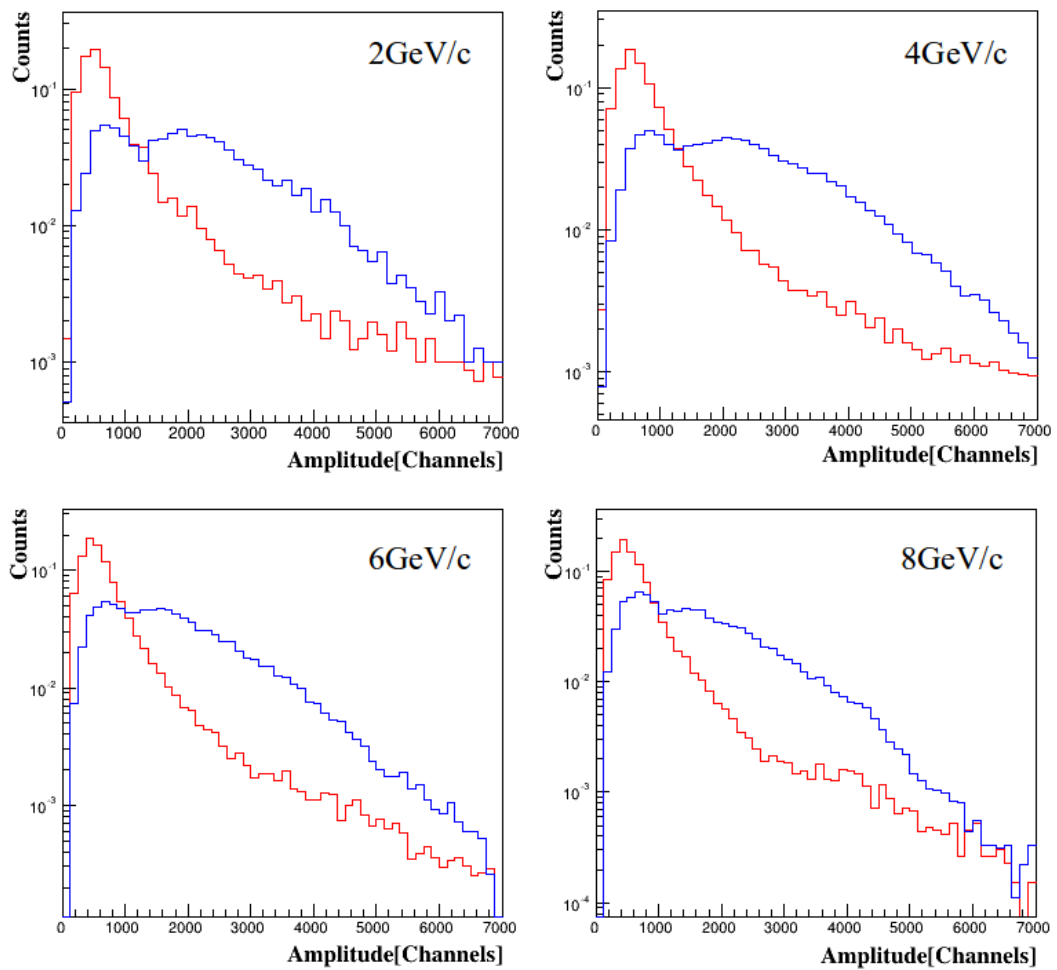


FIGURE 5.17: Pulse height distribution for electrons (blue) and pions (red) at different particle momenta obtained with the 2011 TRD prototype.

produced by electrons in this momentum range in the radiators placed in front of the detector's entrance is mandatory.

The comparison of the energy deposit distributions with radiator and without radiator are shown in Fig.5.18. Both energy deposit distributions, with and without radiator, are almost the same for pions. On the other hand, the distributions with and without radiator are greatly different for electrons. Pions of some GeV are minimum ionizing particles in contrast to electrons, which are already in the Fermi plateau. Therefore, the average electron signal in this momentum region is larger than the pion signal, irrespective of the detector. Since the transition radiation photon is absorbed in the TRD in case of electron events, the mean value and the most probable value of the distributions with radiator are larger than those without radiator. The real size prototype was operated at $HV_a = 2000V$ and $HV_d = 800V$. A regular foil radiator was placed in front of the detector's entrance and trough the chamber a gas mixture of Xe and $CO_2$ was flushed.
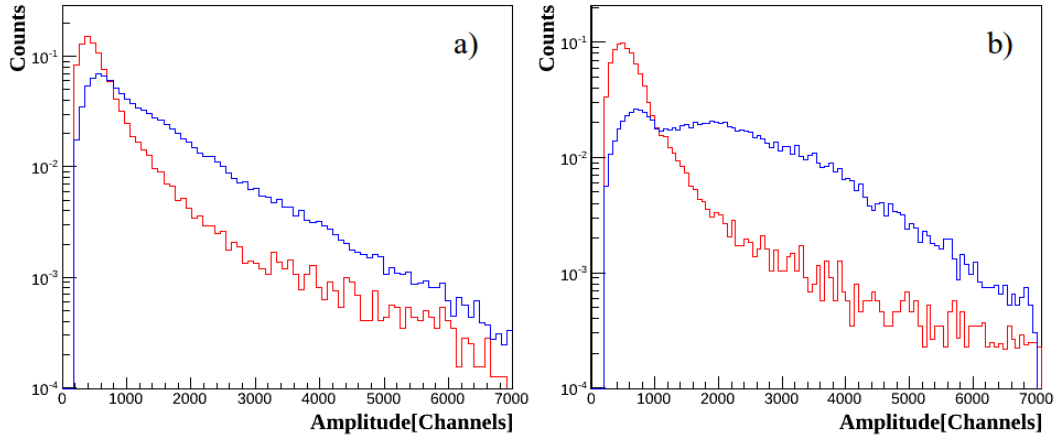


FIGURE 5.18: Comparison of the energy deposit distributions for electrons (blue) and pions (red) without radiator (a) and with radiator (b) obtained with the real size TRD prototype for particle momenta of 3GeV/c.

### 5.3.1 Pion efficiency and pion rejection factor

Pion efficiency, $\epsilon_\pi$, or the pion misidentification probability is used for the evaluation of the electron identification capability of transition radiation prototypes. The pion efficiency is the ratio of pion events in the region bordered by a certain electron efficiency (usually $\epsilon_e$=90%) to the total pion events. The inverse value of the misidentified pions is defined to be the pion rejection factor, given by $\frac{1}{\epsilon_\pi}$.

### 5.3.1.1 The Likelihood method

The normalized charge-deposit distributions of electrons and pions obtained with one detector layer (see Fig.5.19) can be interpreted as probability distributions and used in Monte Carlo simulations in order to determine de pion-rejection factor for the TRD prototypes as a function of the number of detector layers.
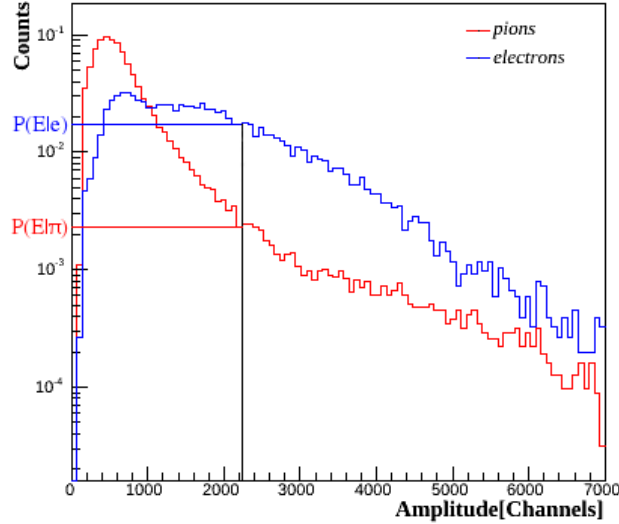


FIGURE 5.19: Normalized pulse height distributions for electrons(blue) and pions(red) and the probability to deposit an energy $E$ for an electron $P(E|e)$ or a pion $P_n(E_n|\pi)$ in a single detector layer.

Electrons and pions have a probability $P(E)$ to deposit the energy $E$ in the detector. Assuming that the measurements are independent, one can extrapolate the pion-rejection factor to $n$ detector layers (in this paper $n{=}10$ layers).

For electrons and pions the deposited energies $E_n^e$ and $E_n^p$ are sampled according to the measured charge-loss spectra in order to determine the probability that this energy $E_n$ is deposited in detector layer $n$ by an electron $P_n(E_n|e)$ or a pion $P_n(E_n|\pi)$. The total probability for an electron to produce a tuple of energy losses $E = E_1, E_2, E_3, ..., E_n$ within $n$ detector layers is:

$$P_e(E) = \prod_{n=1}^{10} P_n(E_n|e) = \prod_{n=1}^{10} P(E_n|e), \tag{5.1}$$

with $P = P^n$ because all $n$ layers, assumed to be identical and independent, are inferred from one (this is permitted since the geometry of all TRD layers will be the same).

The total probability for pions can be calculated correspondingly:

$$P_\pi(E) = \prod_{n=1}^{10} P_n(E_n|\pi) = \prod_{n=1}^{10} P(E_n|\pi) \tag{5.2}$$

With the values for the total probabilities the relative probability $L_e$ or the likelihood to be an electron can be determined:

$$L_e = \frac{P_e(E^e)}{P_e(E^e) + P_\pi(E^e)}, \quad with \quad 0 \le \mathrm{L}_e \le 1 \tag{5.3}$$

The relative probability for a pion to be wrongly identified as an electron is:

$$L_\pi = 1 - L_e = \frac{P_e(E^\pi)}{P_e(E^\pi) + P_\pi(E^\pi)}, \quad with \quad 0 \le \mathrm{L}_\pi \le 1 \tag{5.4}$$

A large number of electron and pion events are obtained from the charge-deposit distributions for the determination of the pion rejection factor, and the likelihood values are filled into a spectrum as shown in Fig.5.20.
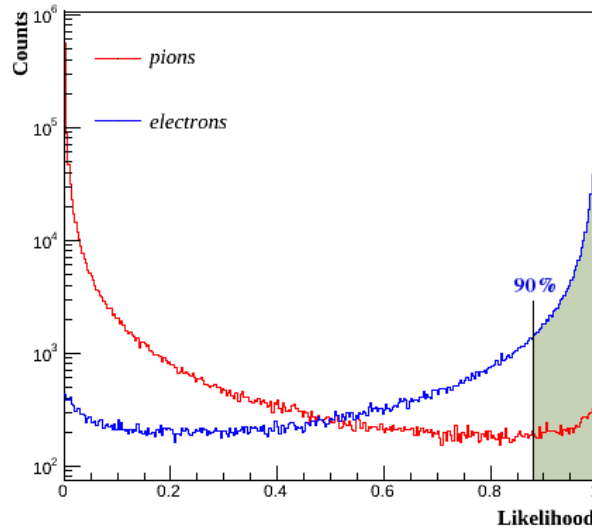


FIGURE 5.20: Likelihood distribution of electrons (blue) and pions (red). The electron entries are integrated from the right until 90% of all electrons are included.

The likelihood distribution of electrons $f^e$ is integrated until the integral includes 90% of the electrons with the highest likelihood values:

$$0.9 = \frac{\int_{L_{\epsilon_e}=90\%}^{1} f^e(L_e)}{\int_0^1 f^e(L_e)}, \tag{5.5}$$

The pion efficiency is the fraction of pions included by the integration limits for 90% of the electrons:

$$\epsilon_\pi = \frac{\int_{L_{\epsilon_e}=90\%}^1 f^\pi(L_e)}{\int_0^1 f^\pi(L_e)} \tag{5.6}$$

In Fig.5.21 the resulting pion efficiency, with 7 detector layers, is shown as a function of particle momenta. As expected the performance decreases with increasing particle energy due to the relativistic rise of pions, the separation between the pions and electrons is reduced as a function of momentum.
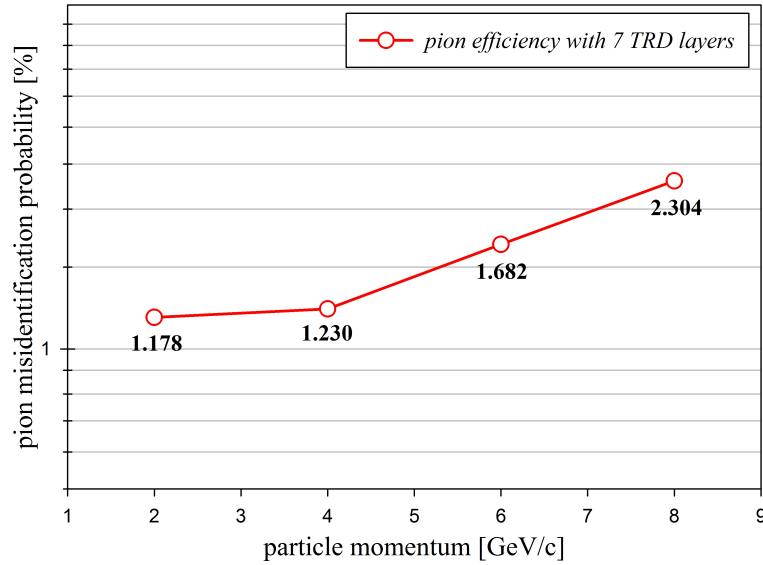


FIGURE 5.21: Pion misidentification probability as a function of particle momentum obtained with 7 TRD layers. The small prototype, TRD1, was operated with Reg2 and the chamber was flushed with a gas mixture of Xe-CO$_2$ (80%-20%), the applied high voltages were $HV_a = 2000V$ and $HV_d = 800V$.

Fig.5.22 and Fig.5.23 show a comparison between the performances obtained with the small TRD prototype build and tested in 2011 as a number of detector layers with different radiators. It is clear that the best performance, $\sim 1\%$ with 7 TRD layers, is obtained with the regular foil radiator when the prototype was operated at $HV_a = 2000V$ and $HV_d = 800V$, for a particle momentum of 2 GeV/c.

The results from the 2012 beam time period are presented in Fig.5.24 and Fig.5.25. A performance of $\sim 1.25\%$ with 6 TRD layers (Fig.5.24) was obtained when the detector was operated with the regular foil radiator, Reg2, and without the Rohacell plate of 3 mm thickness in front of the entrance window.

Fig.5.25 shows that there is almost no difference in pion efficiency irrespective to the method used for signal read-out: from triangular pads (green triangles) or from
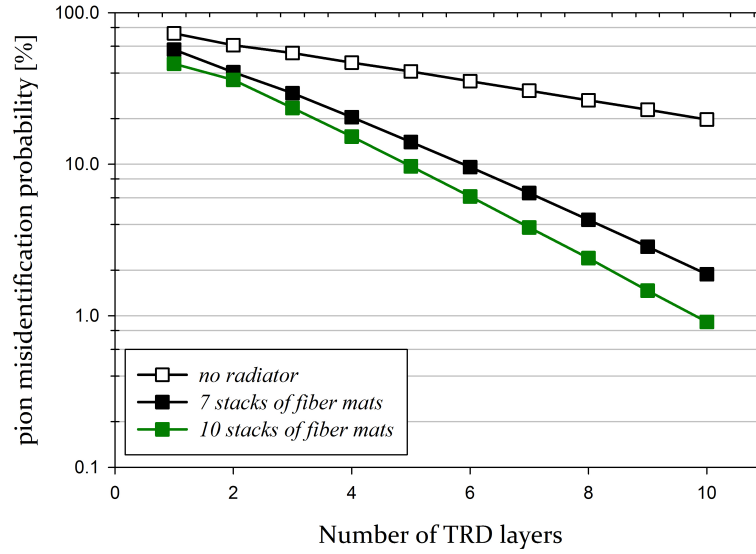
FIGURE 5.22: Comparison between pion efficiency obtained without a radiator (empty circles) and with two types of radiators made from 7 and 10 layers of fibers at a particle mometa of 3GeV/c. The applied voltages were $HV_a = 2000V$ and $HV_d = 600V$.
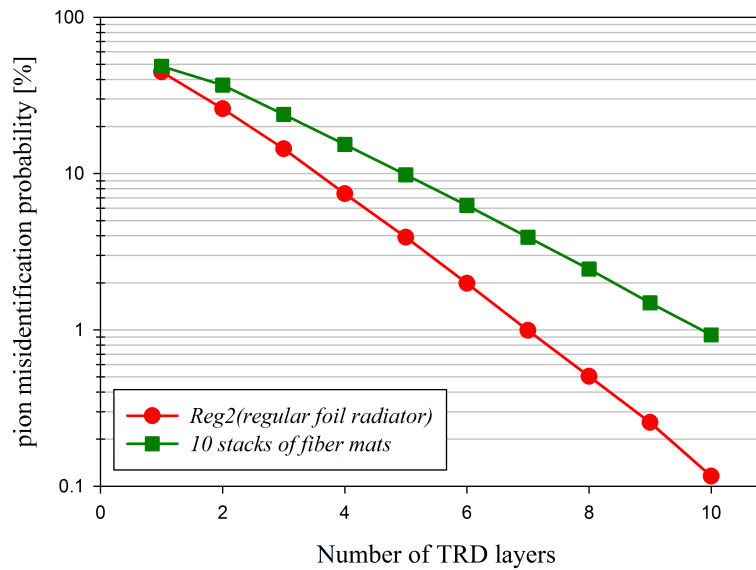


FIGURE 5.23: Extrapolated pion efficiency as a function of detector layers obtained with a fiber radiator (10 stacks of fiber layers) and a regular foil radiator (Reg2) for particle momenta of 2 GeV/c. The best performance, $\sim 1\%$ with 7 TRD layers, is obtained with the regular foil radiator when the prototype was operated at $HV_a = 2000V$ and $HV_d = 800V$
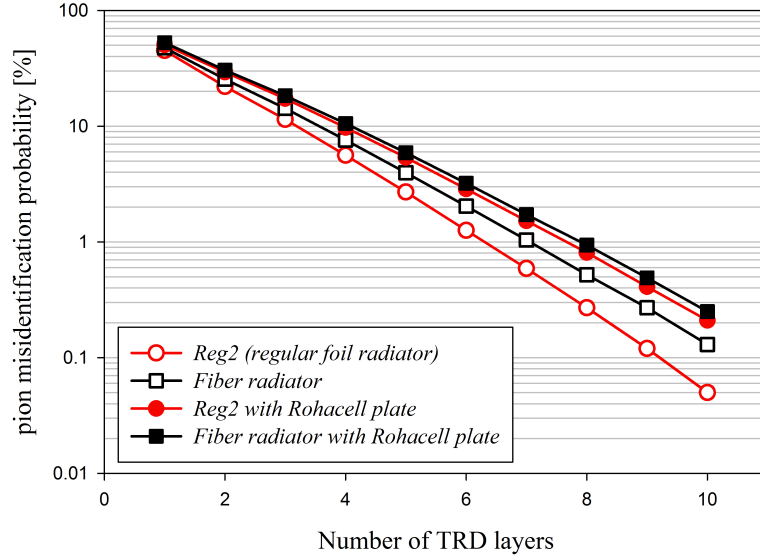
FIGURE 5.24: Extrapolated pion efficiency as a function of detector layers obtained with a fiber radiator (16 stacks of fiber layers) and a regular foil radiator (Reg2) for particle momenta of 3 GeV/c with or without a Rohacell plate of 3 mm thickness in front of the detector entrance. The best performance is of $\sim 1.25\%$ with 6 TRD layers. The prototype was operated at $HV_a = 2000V$ and $HV_d = 800V$, the chamber was flushed with a gas mixture of Xe-CO$_2$ (80%-20%) and the particle momentum was 3 GeV/c.

rectangular pads, obtained by pairing of triangular pads via a special connector (black squares).

Note that the results from Fig.5.24 and Fig.5.25 are from measurements taken during the 2012 beam time, when the aluminized kapton foil has been re-glued with araldite only on the margins of the Rohacell plate and not on the entire plate surface [36] like it was during the 2011 beam time period. The obtained electron-pion discrimination performance of ∼1.25% with 6 layers is consistent with the reported performance of the single-sided TRD prototype build and tested in 2010 [28].

For the real size TRD prototype, the performances in particle discrimination are plotted in Fig.5.26 as a function of the number of detector layers. Of the three radiators (regular foil radiator, fiber radiator and foam radiator) the best performance, $\sim 1\%$ with 6 TRD layers, is obtained with the regular foil radiator. The prototype was operated at $HV_a = 2000V$ and $HV_d = 800V$, for particles with momenta of 3 GeV/c.

Fig.5.27 demonstrates that the electron/pion identification performance is not dependent on the position across the detectors surface, proving that the deformation of the drift electrode due to the slight overpressure of the circulated gas mixture is negligible.
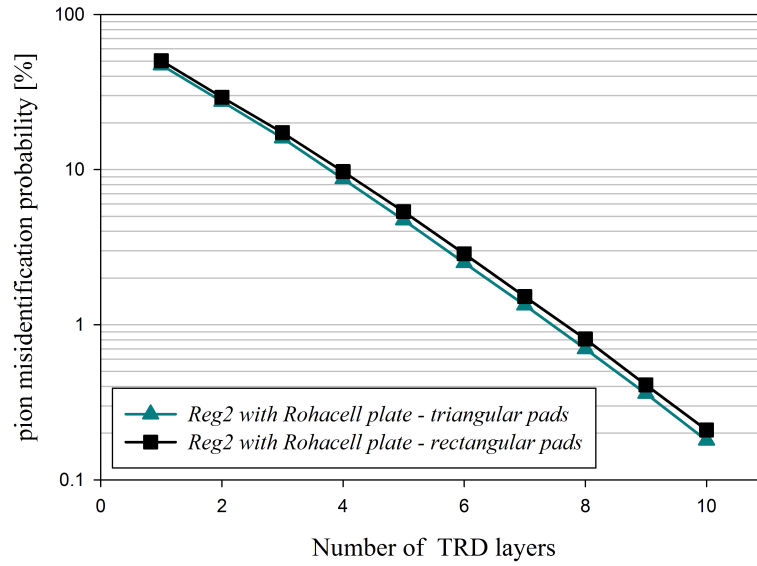
FIGURE 5.25: Pion efficiency obtained for 10 consecutive detector layers. It is shown that there is almost no difference in discrimination performance with the method used for signal read-out: from triangular pads (green triangles) or from rectangular pads (black squares).
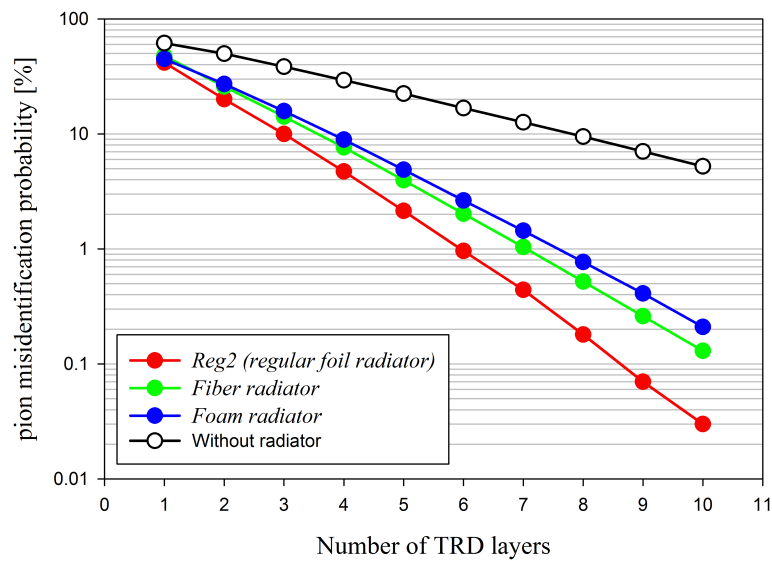


FIGURE 5.26: Comparison between pion efficiency obtained without any radiator (empty symbols) and with three types of radiators: regular foil radiator (red), fiber radiator (green) and foam radiator (blue)
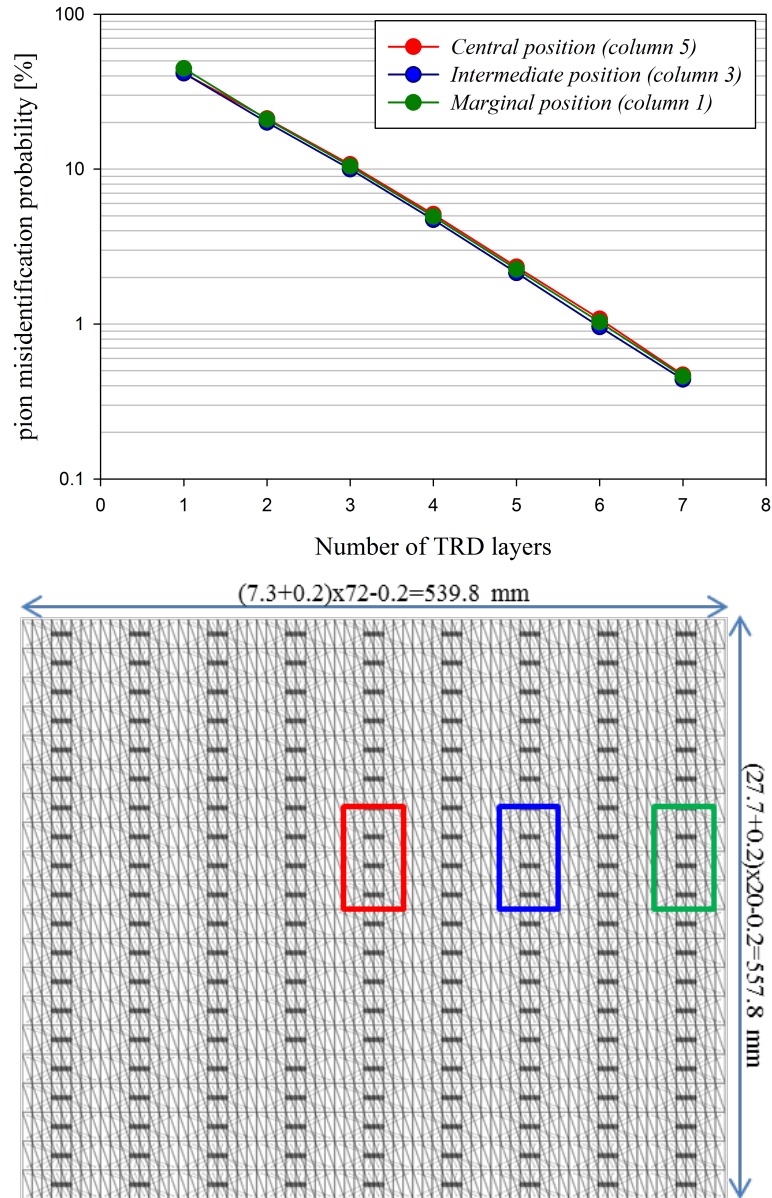
FIGURE 5.27: Extrapolated pion efficiency (upper plot) as a function of position of the illuminated area across the detector's surface (bottom sketch of the read-out electrode structure [34]).

## 5.4 Position Resolution

A charged particle crossing the detector, like electrons, pions and other hadrons, creates a signal via gas ionization as it is described in Chap.3.1.3. In particle tracking, a "hit" represents the induced signal distribution on adjacent read-out pads on the cathode pad plane. With this information and using the Pad Response Function (PRF), the position of the center of a hit can be reconstructed with a resolution better than $1/\sqrt{12}$ times the pad width $W$.

### 5.4.1 The Mathieson parametrisation

Electron avalanches are accelerated in direction of the anode wires and induce an electric charge on the read-out pads. The induced charge distribution depends on the geometric parameters of the chamber and can be used for position information. It's distribution across the pads can be described by an empirical formula proposed by Mathieson. This is a single parameter formula written as [37]:

$$\rho(x/h) = Q_a \cdot K_1 \frac{1 - tanh^2(K_2 \frac{x}{h})}{1 + K_3 h^2(K_2 \frac{x}{h})} \tag{5.7}$$

$$K_1 = \frac{K_2 \sqrt{K_3}}{4 tan^{-1} \sqrt{K_3}} \tag{5.8}$$

$$K_2 = \frac{\pi}{2} \left( 1 - \frac{\sqrt{K_3}}{2} \right) \tag{5.9}$$

where the x-axis is either parallel or perpendicular to the anode wire direction, the value $Q_a$ is the net anode charge, and $h$ is the anode-cathode separation.
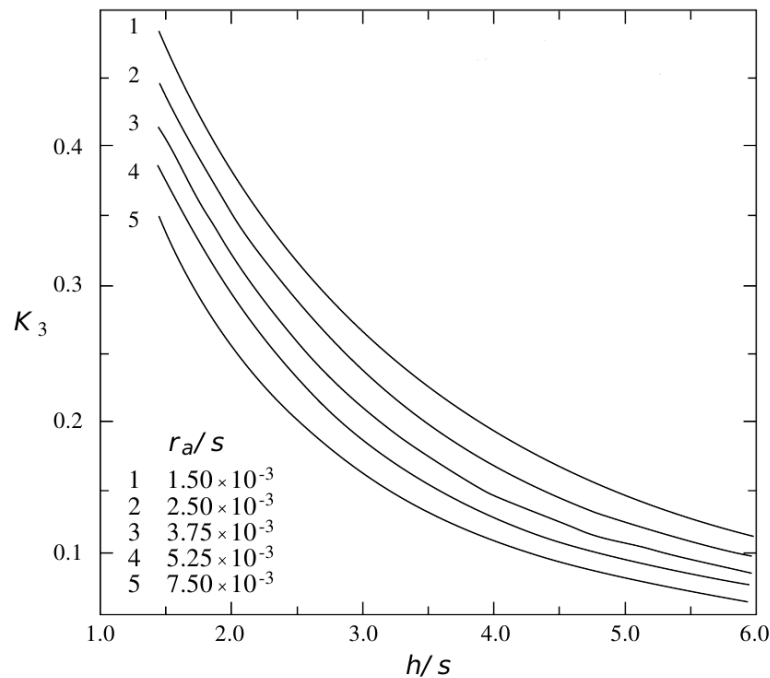


FIGURE 5.28: Values of $K_3$ as a function of chamber parameters $h/s$ and $r_a/s$.

The parameter $K_3$ (see Fig. 5.28) is given for different chamber geometries in Reference [37] as a function of chamber parameters like: the radius of the anode wires $r_a$, the gap between the anode wires $s$, and the anode-cathode separation $h$.

The full width at half maximum (FWHM) of the distribution can be written as:

$$FWHM = h \cdot \frac{4 tanh^{-1}(2 + K_3)^{-1/2}}{\pi \left( 1 - 0.5 K_3^{1/2} \right)} \qquad (5.10)$$

### 5.4.2 Pad Response Function and position reconstruction algorithm

The created avalanches induce a signal on several adjacent pads, effect known as "charge sharing", and provides the possibility of position reconstruction with a finer resolution than the width of a pad. In most cases a signal is distributed among two or three adjacent pads, which are called "2-pad clusters" and "3-pad clusters", respectively.

The degree of charge sharing is measured by the pad response function defined as the ratio of that part of the signal which is induced on a single pad $Q_{pad}$ to the total induced signal $Q_{tot}$ as a function of the distance between the center of the hit and the center of the pad in x-direction.

In the following $i$ is the pad with maximum charge and the displacement $d$ denotes the distance between the centre of the hit and the center of the pad $i$.

If the total signal is approximated to be induced on three adjacent pads and if a Gaussian shape of the PRF is assumed, the PRF can be parametrized as follows [37]:

$$PRF(d) = \frac{Q_{pad}}{Q_{tot}} = \frac{Q_i}{Q_{i-1} + Q_i + Q_{i+1}} = A \cdot exp \left[ -\frac{d^2}{2\sigma^2} \right] \qquad (5.11)$$

where $A$ is the amplitude of the Gaussian function and $\sigma$ is its variance. $Q_i$, $Q_{i-1}$, $Q_{i+1}$ are the charges on the pad with maximum charge $i$ as well as on the neighbouring pads on the left and on the right side, respectively.

Fig.5.29 shows the measured PRF for a small TRD prototype (left) and for the real size prototype (right).

The induced signal on the three adjacent pads caused by a hit having its center at the displacement $d$ is given by:

$$A \cdot exp \left[ -\frac{(W + d)^2}{2\sigma^2} \right] = \frac{Q_{i-1}}{Q_{i-1} + Q_i + Q_{i+1}} \qquad (5.12)$$

$$A \cdot exp \left[ -\frac{d^2}{2\sigma^2} \right] = \frac{Q_{pad}}{Q_{tot}} = \frac{Q_i}{Q_{i-1} + Q_i + Q_{i+1}} \qquad (5.13)$$
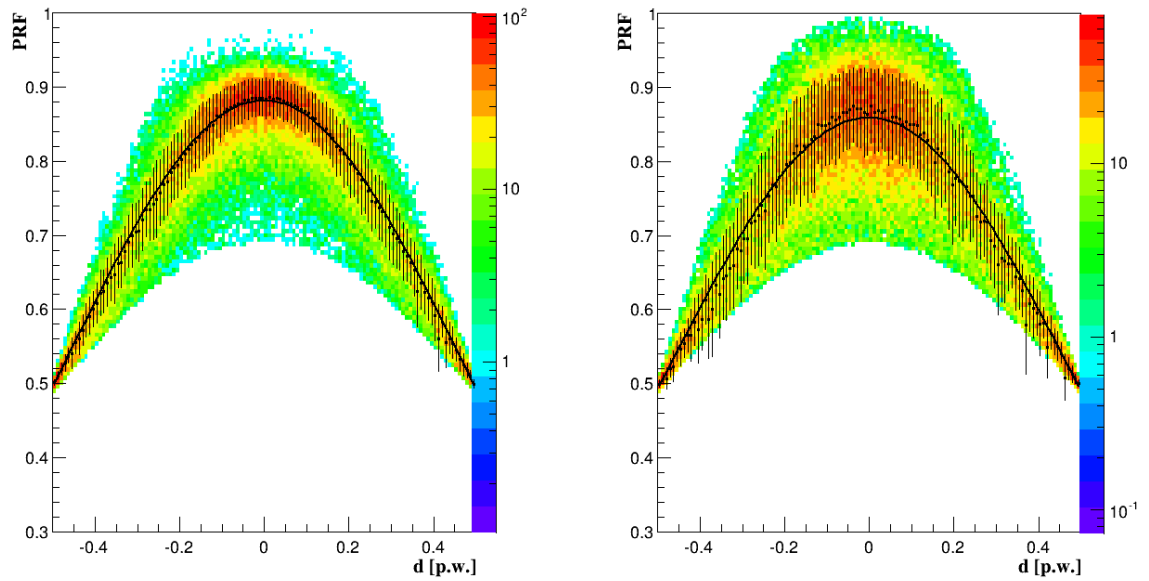
FIGURE 5.29: Pad Response Function for a small prototype (left) and for the real size prototype (right) fitted with a Gaussian function (black line). The obtained values for sigma are: 0.459±3.412e-03 pad widths for the small prototype and 0.469±5.265e-03 pad widths for the real size TRD.

$$A \cdot exp \left[ -\frac{(W - d)^2}{2\sigma^2} \right] = \frac{Q_{i+1}}{Q_{i-1} + Q_i + Q_{i+1}} \tag{5.14}$$

where $W$ is the pad width. The information about the displacement $d$ can be obtained using the signal distribution ( $Q_{i-1}$, $Q_i$, $Q_{i+1}$) without prior knowledge of the variance $\sigma$. If Eq.5.13 is divided by Eq.5.12 and Eq.5.14 by Eq.5.13, it follows:

$$\frac{Q_i}{Q_{i-1}} = exp \left[ \frac{2dW + W^2}{2\sigma^2} \right] \tag{5.15}$$

$$\frac{Q_{i+1}}{Q_i} = exp \left[ \frac{2dW - W^2}{2\sigma^2} \right] \tag{5.16}$$

Two further ratios can be calculated by building the product and the ratio of Eqs.5.15 and Eq5.16:

$$\frac{Q_{i+1}}{Q_{i-1}} = exp \left[ \frac{2dW}{\sigma^2} \right] \tag{5.17}$$

$$\frac{Q_i^2}{Q_{i-1} \cdot Q_{i+1}} = exp \left[ \frac{W^2}{\sigma^2} \right] \tag{5.18}$$

By insertion of Eq.5.17 in Eq.5.18 and solving for $d$ an expression independent of $\sigma$ for $d$ is found:

$$d = \frac{W}{2} \cdot \frac{ln\left(\frac{Q_{i+1}}{Q_{i-1}}\right)}{ln\left(\frac{Q_i^2}{Q_{i-1} \cdot Q_{i+1}}\right)} \tag{5.19}$$

In the case of 2-pad clusters, the charge is shared only between two adjacent pads, the displacement and thus the position can be determined by using Eq.5.20 (in the case of signals on pad i and i 1) and Eq.5.21 (in the case of signals on pad i and i + 1).

$$d = \frac{\sigma^2}{W} \cdot ln\left(\frac{Q_i}{Q_{i-1}}\right) - \frac{W}{2} \tag{5.20}$$

$$d = \frac{\sigma^2}{W} \cdot ln\left(\frac{Q_{i+1}}{Q_i}\right) + \frac{W}{2} \tag{5.21}$$

In most cases, the signal is shared on three adjacent pads and the best results are obtained by combining Eqs.5.20 and Eq.5.21 in a weighted average with weights $Q_{i-1}^2$ and $Q_{i+1}^2$ [21], resulting:

$$d = \frac{1}{Q_{i-1}^2 + Q_{i+1}^2} \left\{ Q_{i-1}^2 \left[ \frac{\sigma^2}{W} \cdot ln\left(\frac{Q_i}{Q_{i-1}}\right) - \frac{W}{2} \right] + Q_{i+1}^2 \left[ \frac{\sigma^2}{W} \cdot ln\left(\frac{Q_{i+1}}{Q_i}\right) + \frac{W}{2} \right] \right\} \tag{5.22}$$

where $\sigma$ is the width of the Gaussian fitted to the experimental pad response function and $W$ is the pad width.

Being aware of the displacement the cluster position can be reconstructed in both coordinates, $x$ and $y$, using a simple algorithm which uses two methods of pairing two adjacent triangular pads, method presented in Fig.5.30 :
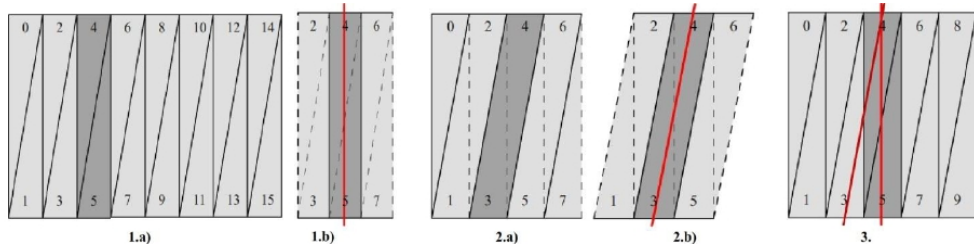


FIGURE 5.30: Position reconstruction algorithm: 1. on rectangular pads; 2. on diagonal pads; 3. cluster position in both coordinates.

1.a) each two adjacent triangular pads are paired in order to obtain a rectangular pad; the rectangular pad with maximum charge is found (see Fig.5.31 - left);
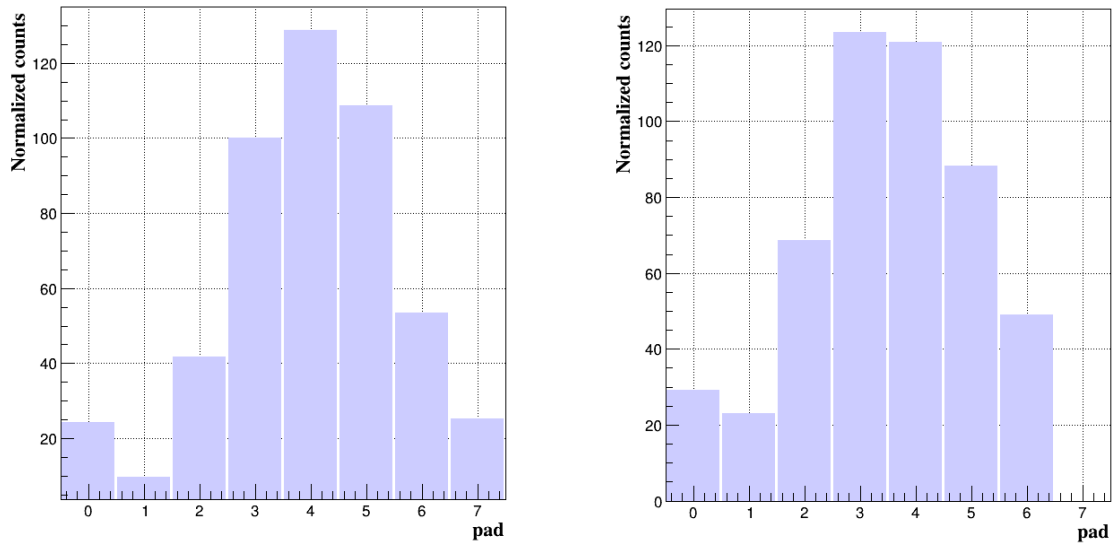


FIGURE 5.31: Beam profile for TRD1: the position of the pad with maximum charge for the rectangular pairing of triangular pads (left) and for the diagonal pairing of triangular pads (right).

1.b) the horizontal displacement $d_h$ between the cluster position and the center of the rectangular pad is calculated in order to obtain the $x_\perp$ coordinate;
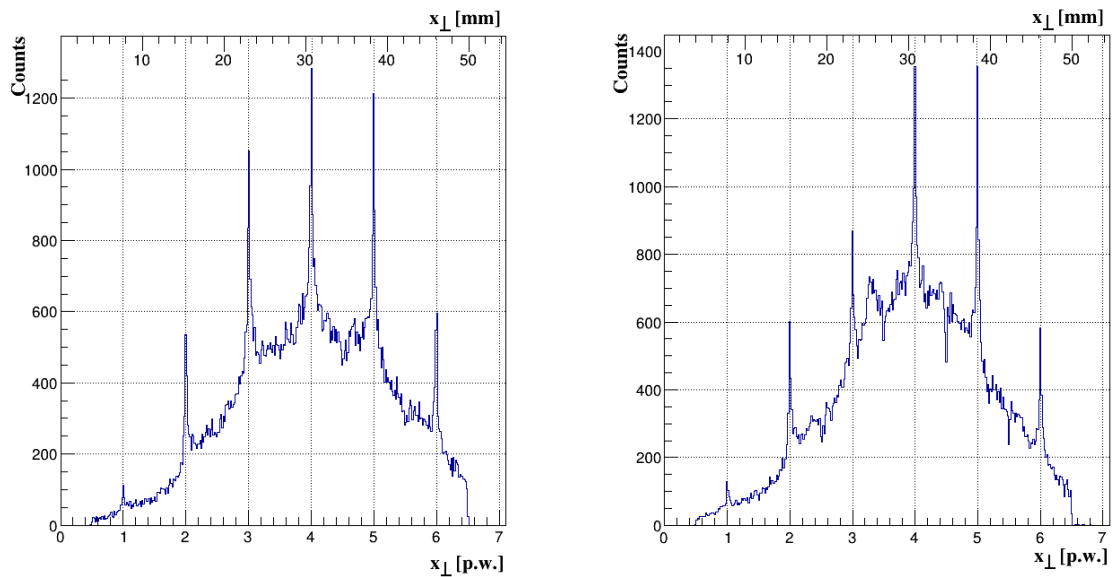


FIGURE 5.32: Reconstructed position across the rectangular pads, $x_\perp$ coordinate, for TRD1 (left) and for TRD2 (right).

2.a) each two adjacent triangular pads are paired in order to obtain a diagonal pad; the diagonal pad with maximum charge is found (see Fig.5.31 - right);

2.b) the diagonal displacement $d_d$ between the cluster position and the center of the diagonal pad is calculated in order to obtain the $x_/$ coordinate;
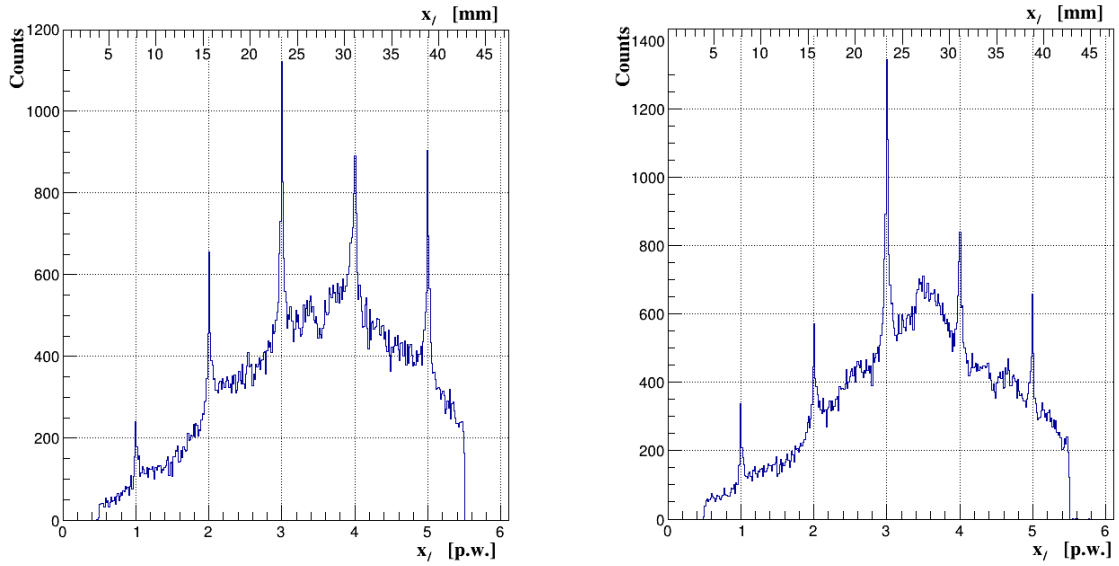


FIGURE 5.33: Reconstructed position across the diagonal pads, $x_/$ coordinate, for TRD1 (left) and for TRD2 (right).

3. the intersection of both displacements gives the reconstructed position of the cluster in the y coordinate.
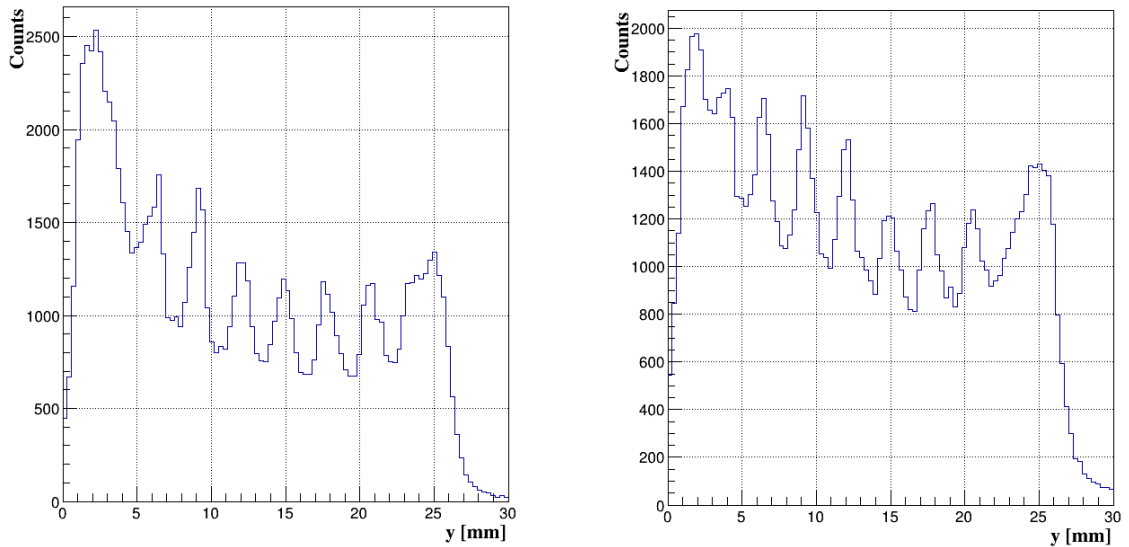


FIGURE 5.34: Reconstructed position along the pads, $y$ coordinate, for TRD1 (left) and for TRD2 (right). The peaks correspond to the wire positions which are shifted.

The border pads (0 and 7 for the rectangular pad system; 0 and 6 for the diagonal pad system) have to be excluded to be the pad with maximum charge $Q_i$ during the
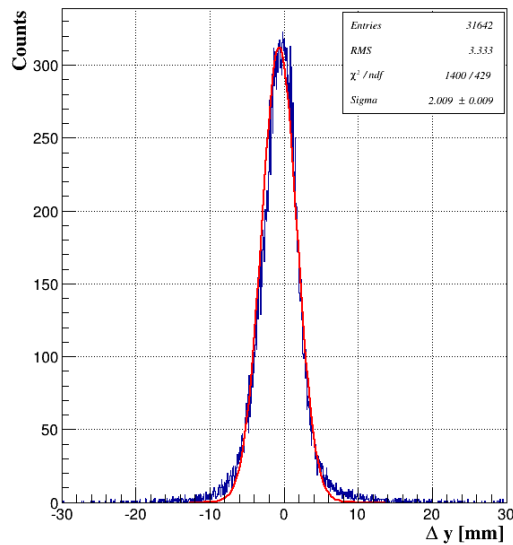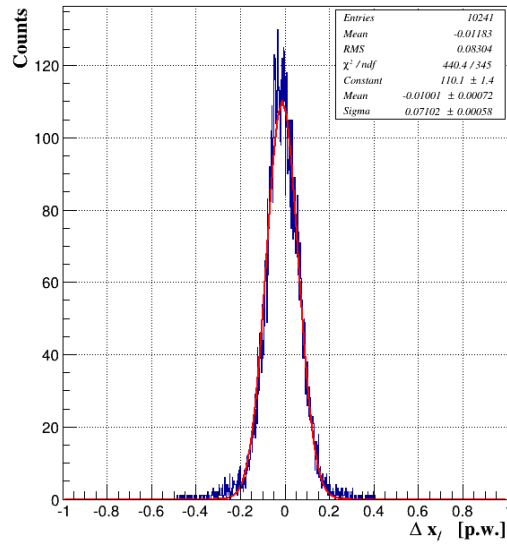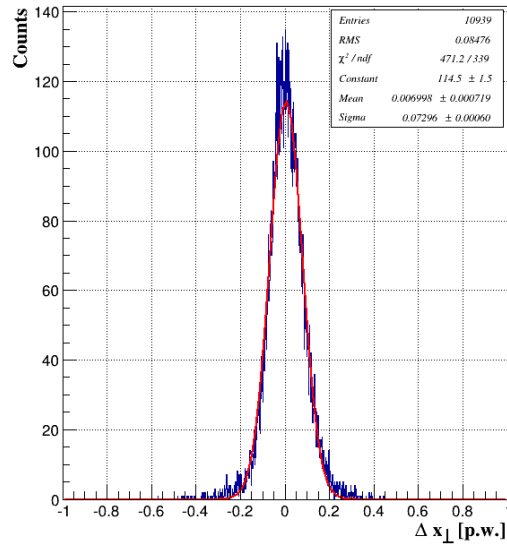
FIGURE 5.35: Position resolutions across the pads obtained for the rectangular pad system (top) and for the diagonal pad system (middle), and along the pads (bottom).

position reconstruction analysis in order to have the signal on three neighbouring pads.

The $x$ coordinate (see Fig.5.32 and Fig.5.33) for both TRD1 and TRD2 can be determined knowing the displacement $d$ between the cluster position and the center of the rectangular/diagonal pad:

$$x = d + (i + \frac{1}{2}) \cdot W \tag{5.23}$$

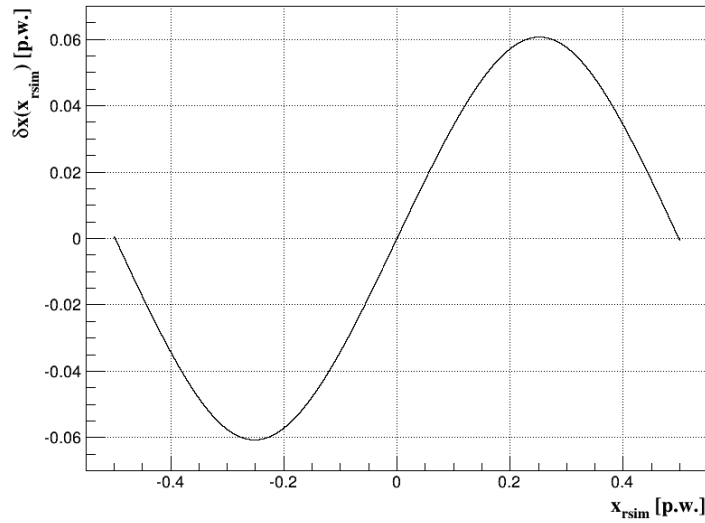where $i$ is the pad with maximum charge and $W$ is the pad width.



FIGURE 5.36: Systematic errors in position reconstruction.

The peaks within the spectra located in the pad center are due to the algorithm systematics [38]. The used algorithm for position reconstruction is a well known method involving linear relations between charge fractions and the coordinate. It is known however that the difference $\delta x(x_{rsim}) = x_{rsim} - x_{sim}$, where $x_{sim}$ is a simulated hit position across the pads and $x_{rsim}$ is the reconstructed position of the simulated event using this method, exhibits a periodic structure along the pad with zero mean only at the middle point and at the end-points of the pad (see Fig.5.36).

The position resolution across the pads (see Fig.5.35) is the standard deviation obtained by fitting the difference between the reconstructed hit positions in TRD1 and TRD2 ($\Delta x = x_{TRD1} - x_{TRD2}$). Assuming equal contribution of both chambers the obtained position resolution is $\sigma_{x_\perp}/\sqrt{2} = 0.073 \pm 0.0006$ pad widths ($\sigma_{x_\perp} \simeq 360$ $\mu$m) and $\sigma_{x_/}/\sqrt{2} = 0.071 \pm 0.0006$ pad widths ($\sigma_{X_/} \simeq 351$ $\mu$m).

Due to the special geometry of the read-out electrode it is possible to obtain the hit position along the pads for each detector layer using Eq.5.24. Fig.5.34 shows, for
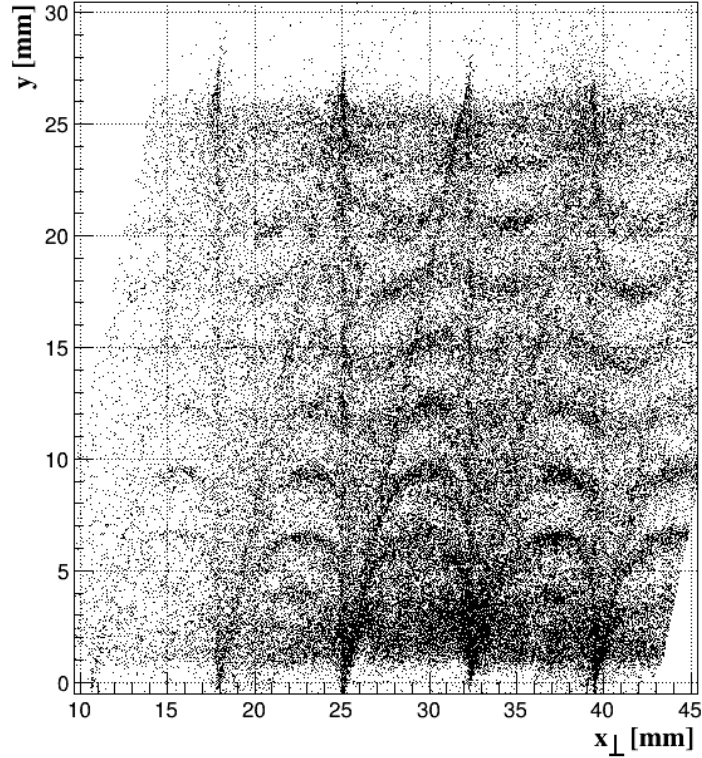
FIGURE 5.37: Hit position reconstructed in both coordinates (x, y).

both TRD prototypes, the reconstructed hit positions along the pads. The peaks in the distributions are caused by high field gradients near to the anode wires. The displacement between the peaks is caused by the position of the wires which are not accurately symmetric to the pad rows.

$$y = x_\perp \cdot tg(\alpha) + \frac{x_/ - x_\perp \sqrt{tg^2(\alpha) + 1}}{sin(\alpha)} \qquad (5.24)$$

where $\alpha = arctg(W/H)$, $H$ is the pad height.

The reconstructed hit position in both coordinates (x, y) in one detector layer is represented in Fig.5.37. In this representation, the influence of the anode wires and of the method systematics can be seen clearly as sinusoidal structures along and across the pads. The triangle pattern is due to the pairing of triangular pads in rectangular and diagonal pads and because of the $y(x_\perp, x_/)$ dependency.

By fitting with a Gaussian function the distribution from Fig.5.35 obtained in a similar way as for the resolution across the pads an average value for the position resolution of the hit of $\sigma_y/\sqrt{2} = 2.009 \pm 0.0009$ mm is obtained ($\sigma_y \simeq 1.420$ mm).

# Chapter 6

# Conclusions/Summary

The focus of this thesis was the development of a Transition Radiation Detector (TRD) designed to meet the requirements of the TRD subdetector of the future CBM experiment at FAIR. Within the CBM experiment, the TRD subsystem will provide electron identification and together with a Silicon Tracking System (STS) will allow tracking of charged particles. In conjunction with the Ring Imaging Cherenkov (RICH) detector and a time-of-flight (TOF) measurement, it will provide sufficient electron identification for the measurements of charmonium and low-mass vector mesons. The most important and challenging aspect of the TRD design is that the detector has to cope with very high interaction rates of up to $10^7$ Hz and large particle multiplicities. These conditions lead to counting rates of up to 100 kHz/cm$^2$ in the central part of the TRD (at small polar angles).

Three prototypes, two small chambers and one of similar size as the final design of the TRD chambers to be used at small polar angles, were designed, built and tested within the group of Prof. M. Petrovici from Hadron Physics Department National Institute for Physics and Nuclear Engineering Bucharest, Romania. The chambers are based on a single-sided architecture retained from a previous small prototype [28] but have a read-out electrode characterized by a much smaller pad size (1 cm$^2$ pad area).

The position resolution and electron-pion-separation performance of the TRD prototypes were investigated during beam tests at CERN and in $^{55}$Fe X-ray source measurements performed in the laboratory of the Hadron Physics Department (real size prototype). Also, during the X-ray source tests a special attention was given to the characterization and calibration of the electronic channels obtaining finally an energy resolution of $\sim 8.196\%$ for 5.9 keV X ray line of $^{55}$Fe.

Using data from in-beam measurements, the electron identification capability of the TRD prototypes was estimated by determining the pion efficiency, $\epsilon_\pi$, using the Likelihood method. The pulse-height distributions of electrons and pions were used as probability distributions in Monte Carlo simulations in order to obtain the pion rejection factor of the prototypes as a function of number of TRD layers: the pion efficiency was determined for one TRD layer and then subsequently extrapolated to a larger number of layers. The pion efficiency of $\sim 1\%$ at an electron efficiency of 90%, was achieved for six layers of the prototypes. This performance was reached by using a regular foil radiator and satisfies the requirement of the CBM-TRD. From the momentum dependence of pion rejection, pion rejection capability decreases with increasing particle momentum. This is because the energy loss of pions is larger with increasing momentum, while the electron energy loss and TR yield is almost constant for all momenta.

The position resolution was determined using two identical small prototypes assuming equal contribution of both chambers. A position resolution across the pads (x coordinate) of $\sim 355.5$ $\mu$m and a position resolution along the pads (y coordinate) of $\sim 1.4$ mm was measured.

In summary, the obtained results demonstrate that a TRD detector with six layers based on this type of architecture and regular radiator fulfils the required electron/pion discrimination performance of CBM experiment and can provide an efficient tracking with the desired resolution. In the future detailed investigations of the chamber performance in high counting rate irradiation on the whole active area and multi-hit environment similar to those expected in experiments at FAIR are foreseen.

# Bibliography

[1] Summary Tables of Particle Physics . URL `http://pdg.lbl.gov/2011/download/rpp-2010-booklet.pdf`.

[2] J. C. Collins and M. J. Perry, Superdense Matter: Neutrons or Asymptotically Free Quarks? *Phys. Rev. Lett.*, 34:1353–1356, 1975.

[3] Bag Model of Quark Confinement. URL `http://hyperphysics.phy-astr.gsu.edu/hbase/particles/qbag.html`.

[4] T. Nakamura, Experimental study on QCD phase transition by measuring charged particle density correlations in Au+Au collisions at $\sqrt{S_{NN}}$=200gev. 2009.

[5] F. Karsch et al, Quark mass and flavour dependence of the QCD phase transition. *Nucl. Phys.*, B 605:579–599, 2001.

[6] H. Stcker and W. Greiner, Dynamics of the hadronization phase transition at finite baryon chemical potentials. *Phys. Lett.*, B 173:468–472, 1986.

[7] V.D. Toneev et al, Three-Fluid Simulations of Relativistic Heavy-Ion Collisions. *nucl-th/0309008*, 2003.

[8] Z. Fodor and S.D. Katz, Critical point of QCD at finite T and $\mu$, lattice results for physical quark masses. *hep-lat/0402006*, 2004.

[9] S. Ejiri et al, Study of QCD thermodynamics at finite density. *hep-lat/031*, 2006.

[10] C. Klein-Bösing, *Production of Neutral Pions and Direct Photons in Ultra-Relativistic Au+Au Collisions.* PhD thesis, Institut für Kernphysik, Westfülische Wilhelms-Universitüt Münster, 2005.

[11] P. Braun-Munzinger, Chemical Equilibration and the Hadron-QGP Phase Transition. *Nucl. Phys.*, A681:119, 2001.

[12] K. Fukushima and T. Hatsuda, The phase diagram of dense QCD. *Rept. Prog. Phys.*, 2011.

[13] V.D. Toneev B. Friman, W. Nrenberg, *Eur. Phys. J.*, A3:165, 1998.

[14] CBM experiment . URL `hhttp://www.gsi.de/fair/experiments/CBM/`.

[15] D. Emschermann, Status of CBM TRD geometry v13a, January 2013. URL `http://cbm-wiki.gsi.de/cgi-bin/view/TRD/CbmTrdMeeting20130116`.

[16] Cyrano Bergmann,  Beam test results of Münster TRD 2012 prototypes, March 2013.  URL `https://indico.gsi.de/getFile.py/access?contribId=4&sessionId=20&resId=0&materialId=slides&confId=1912`.

[17] W. Blum, W. Riegler, and L. Rolandi, *Particle Detection with Drift Chambers, 2nd edition.* Springer-Verlag, 2008.

[18] J. Anthony Seibert, X-Ray Imaging Physics for Nuclear Medicine Technologists. Part 1: Basic Principles of X-Ray Production. *JNMT*, 32 no. 3:139–147, 2004.

[19] C. Grupen, *Teilchendetektoren.* BI-Wiss.-Verl., 1993.

[20] C. Amsler et al, Transition radiation from relativistic electrons in periodic radiators. *Phys. Lett.*, B 667:1, 2008.

[21] W. Blum and L. Rolandi, *Particle Detection with Drift Chambers.* Springer-Verlag, 1994.

[22] M. Cherry et al, Transition radiation from relativistic electrons in periodic radiators. *Phys. Rev.*, D 10:35–94, 1974.

[23] M. Klein-Bösing, *Development of a Transition Radiation Detector and Reconstruction of Photon Conversions in the CBM Experiment.* PhD thesis, Institut für Kernphysik, Westfülische Wilhelms-Universitüt Münster, 2009.

[24] D. Green, *The Physics of Particle Detectors.* Cambridge University Press, 2009.

[25] Interactions of Photons in Matter, 2001.  URL `http://mightylib.mit.edu/Course%20Materials/22.01/Fall%202001/photons%20part%202.pdf`.

[26] Law of Energy Conservation and the Doppler Effect .  URL `http://www.relativitycalculator.com/energy_doppler.shtml`.

[27] ALICE Collaboration, A Transition Radiation Detector, Technical Design Report. Technical report, 2001.

[28] M. Petris et al, Single Sided TRD prototype. *CBM Progress Report*, page 46, 2011.

[29] M. Petris et al  e/$\pi$ Identification and position resolution of double sided TRDs. *CBM Progress Report*, page 48, 2011.

[30] M. Petrovici et al, Update on CBM-TRD prototypes tests @ PS-CERN, September 2011. URL `https://indico.gsi.de/getFile.py/access?contribId=1&sessionId=10&resId=0&materialId=slides&confId=1119`.

[31] Radulescu Laura, Drawing by Radulescu Laura.

[32] A. Caragheorgheopol, D. Bartos, and V. Catanescu, Preliminary results of tests on TRD Front-End Prototype Chip, October 2009. URL `http://niham.nipne.ro/DOC-2009-Oct-155-1_FEE_Split.pdf`.

[33] T. Armbruster et al, *CBM Progress Report*, page 45, 2010.

[34] Victor Simion, Drawing by Victor Simion.

[35] M. Tarzila et al, Two dimensionally position sensitive real size CBM-TRD prototype. *CBM Progress Report*, page 60, 2013.

[36] M. Tarzila, Preliminary results of 2011 CBM TRD Test-Beam @ CERN, March 2011. URL `https://indico.gsi.de/getFile.py/access?contribId=0&sessionId=9&resId=0&materialId=slides&confId=1368`.

[37] E. Mathieson, Cathode charge distributions in multiwire chambers. *Nuclear Instruments and Methods in Physics Research*, A270:602–603, 1988.

[38] M. Tarzila, electron/pion rejection performance and systematic studies of position resolution of Bucharest TRD prototype. URL `https://indico.gsi.de/getFile.py/access?contribId=85&sessionId=7&resId=1&materialId=slides&confId=1369`.